Available online at www.sciencedirect.com

ScienceDirect

Geochimica et Cosmochimica Acta 282 (2020) 227–244

Geochimica et Cosmochimica Acta

www.elsevier.com/locate/gca

Laminated soil carbonate rinds as a paleoclimate archive of the Colorado Plateau

T.E. Huth [a,*], T.E. Cerling [b], D.W. Marchetti [c], D.R. Bowling [d], A.L. Ellwein [e], B.H. Passey [a], D.P. Fernandez [b], J.W. Valley [f], I.J. Orland [f,g]

[a] Department of Earth and Environmental Sciences, University of Michigan, Ann Arbor, MI 48109, USA
[b] Department of Geology and Geophysics, University of Utah, Salt Lake City, UT 84112, USA
[c] Department of Natural and Environmental Science, Western Colorado University, Gunnison, CO 81231, USA
[d] School of Biological Sciences, University of Utah, Salt Lake City, UT 84112, USA
[e] Rocky Mountain Biological Laboratory, Crested Butte, CO 81224, USA
[f] Department of Geoscience, University of Wisconsin-Madison, Madison, WI 53706, USA
[g] Wisconsin Geological and Natural History Survey, University of Wisconsin-Madison, Madison, WI 53705, USA

Received 13 December 2019; accepted in revised form 20 May 2020; Available online 29 May 2020

Abstract

Recent work suggests that the C- and O-isotope composition of laminated soil carbonate rinds can provide high-resolution (100 s yr/sample) information about hydrologic processes and vegetation over tens of thousands of years. However, while this archive can potentially provide quantitative reconstructions, most interpretations have thus far been qualitative. In this study, we show how modern soil data and "clumped" isotope paleothermometry can be leveraged to constrain the conditions of rind formation for a sample from the western Colorado Plateau, Utah, USA. We can thus quantitatively interpret rind isotope values as vegetation composition (%C_3–plants) and soil water oxygen isotope composition ($\delta^{18}O_{soil-water}$) over 35–5 ka. We validate the approach by demonstrating consistency between our record and other paleoarchives from the western USA. Laminated soil carbonate rinds therefore represent a new avenue for sub-millennial scale, quantitative investigations of paleoclimatology, paleoecology, archeology, and modeling questions down to the level of individual soils.

Keywords: Laminated soil carbonate rind; Carbon and oxygen isotopes; Quaternary; Colorado Plateau; North American Monsoon; Radiocarbon; Secondary Ion Mass Spectrometry

1. INTRODUCTION

Soil carbonate ($CaCO_3$) forms in drylands of the world and has been extensively used as a paleoarchive. This is because its stable isotope composition (C and O) can be tied to environmental conditions at the time of formation (Cerling, 1984). Soil carbonate carbon isotope composition ($\delta^{13}C$) is primarily related to that of soil CO_2 via the photosynthetic pathway of organic material being respired and soil respiration rate during mineral formation (Cerling, 1984). For example, studies have interpreted $\delta^{13}C$-soil carbonate data (hereafter, $\delta^{13}C_{sc}$) in terms of landscape vegetation composition because plants using the C_3 and C_4 photosynthetic pathways are isotopically distinct. However, respiration rate is also an important consideration because soil CO_2 comes from two sources: biological respiration and the atmosphere. The abundance of soil CO_2 from each source can be described using a diffusion transport model (Cerling, 1984; Davidson, 1995).

* Corresponding author.
E-mail address: tehuth@umich.edu (T.E. Huth).

https://doi.org/10.1016/j.gca.2020.05.022
0016-7037/

Thus, there exists a quantitative relationship between $\delta^{13}C_{sc}$ and plant composition.

The oxygen isotope composition of soil carbonate ($\delta^{18}O_{sc}$) is related to that of soil water ($\delta^{18}O_{soil-water}$) and the temperature of formation (Cerling, 1984). Soil water in turn is the result of meteoric precipitation and soil processes (e.g., evaporation, transpiration, mixing, etc.), both of which vary through time and influence $\delta^{18}O_{soil-water}$. As with the relationship between $\delta^{13}C_{sc}$ and $\delta^{13}C_{soil-CO2}$, there exists a quantitative relationship between $\delta^{18}O_{sc}$ and $\delta^{18}O_{soil-water}$ (and ultimately $\delta^{18}O_{rain}$ and $\delta^{18}O_{snow}$). Interpreting $\delta^{18}O_{sc}$ in terms of $\delta^{18}O_{soil-water}$ is feasible as long as the temperature of mineral formation can be constrained (Kim and O'Neil, 1997). Estimating $\delta^{18}O_{rain}$ from $\delta^{18}O_{sc}$ is more complicated as modifying soil processes are more difficult to constrain (e.g., Breecker et al., 2009; Cerling, 1984; Oerter and Amundson, 2016; Quade, 2014; Quade et al., 1989; Huth et al., 2019).

The relationships between soil carbonate isotope composition, vegetation type, and climate have been extensively used for paleoclimate and paleoecology research. In general, applications have focused on questions involving change on $>$ 0.1–1 Ma timescales. This is because most studies utilize soil carbonate in the form of nodules, which due to their complicated internal age structure are generally conducive to bulk estimates of environmental conditions for the life of the soil (e.g., 1–100 s ka). As soil formation periods are generally of the same order of magnitude or greater than the duration of most late Quaternary climate fluctuations, there have been considerably fewer applications of soil archives to these shorter timescales as compared to speleothems and lake cores (e.g., Quade, 2014; Birkeland et al., 1991; but see also the stacked paleosols of the Chinese Loess Plateau; e.g., Sun et al., 2006). The few soil studies available have used bulk isotopic measurements in (paleo-)soil sequences to infer 1–10 kyr environmental changes (Cole and Monger, 1994; Liu et al., 1996). To acquire high-resolution (100 s yr/sample) records of late Quaternary climate and vegetation change, recent studies have focused on soil carbonate formed as laminated rinds on the bottoms of clasts (hereafter "rinds," but see also the use of "pedothems" by Oerter et al., 2016). Rinds are a desirable record type because they frequently preserve an intact, dateable stratigraphy, record 10–100 s kyr of change, are common in arid and semi-arid regions worldwide, provide a definitively local signal, and allow for identification of changes in vegetation and climate/soil conditions from a single, internally consistent record (Oerter et al., 2016; Huth et al., 2019; Cerling, 1984). Therefore, in addition to providing an independent view of climate and vegetation change, rinds can potentially provide 10 s kyr of high-resolution (100 s yr/sample), paleoclimate data over a range of elevations.

The basic effectiveness of laminated rinds as a proxy has been explored by researchers in Wyoming, Syria, Turkey, and Siberia (Oerter et al., 2016; Pustovoytov et al., 2007a, 2007b) as well as by our group working in Utah (Huth et al., 2019). These researchers used a variety of methodologies to date (radiocarbon vs. U/Th dating) and sample [hand drilling, micromilling, Secondary Ion Mass Spectrometry (SIMS)] rinds of mm to $>$ 10 cm thickness. Study landforms varied considerably, encompassing river terraces, debris flows, alluvial fans, and archeological sites (stone construction and pottery sherds).

While previous studies have emphasized the potential for rinds to provide sub-millennial scale paleoclimate and paleovegetation information, most interpretations have thus far been necessarily qualitative. This is because previous studies lacked direct information about the timing and conditions of soil carbonate formation today and in the past. As the timing of soil carbonate formation is seasonally biased (Huth et al., 2019; Oerter and Amundson, 2016; Breecker et al., 2009; Kelson et al., 2020), without constraining the (1) temperature and (2) soil respiration (i.e., autotrophic plus heterotrophic respiration) during mineral formation, it was challenging for previous researchers to quantitatively interpret the records.

In this study, we build upon previous work using soil carbonate rinds by demonstrating a methodology to obtain quantitative estimates of past $\delta^{18}O_{soil-water}$ and vegetation composition ($\%C_3$–plants) from a soil carbonate rind. We explored the proxy at one site on the Colorado Plateau and provide a detailed record of climate and vegetation change (100 s yr resolution over 35–5 ka). First, we describe the study setting, our prior work constraining the modern timing of soil carbonate formation, the paleorecord sampling strategy, and the methodology for reconstructing paleoclimate and vegetation change. We then present the results, discuss the validity of our interpretations in the context of previous paleoclimate and vegetation inferences, and conclude with an outlook for the methodology.

2. STUDY SETTING AND METHODOLOGY

Because a primary motivation of this study is to describe a new methodology, we focus here on the portions of the study design, sample analyses, and methodology relevant to reconstructing $\delta^{18}O_{soil-water}$ and vegetation composition through time. Full details of the sample analyses can be found in the Supplementary Appendix.

2.1. Climate and geologic setting

The Fremont River Valley, which contains the town of Torrey, Utah, USA, has a semiarid climate, receiving ≈260 mm of annual precipitation (Prism Climate Group, 2018) (Fig. 1; SI Appendix, Fig. S1). Meteoric precipitation is seasonally biased (45 % in JASO) with summer rainfall derived from southerly winds usually associated with the North American Monsoon (NAM, Higgins et al., 1997). NAM related rainfall may be orographically enhanced by the site's location between mountain ranges to the north and south. Winter precipitation is brought by cold frontal storms associated with westerly winds. Temperature seasonality is large at Torrey; average daily temperature (average low/high) in January and July are −3.7 °C (-11.3/3.9 °C) and 20.2 °C, (11.4/28.9 °C), respectively.

The study area features a number of soils developed on stable mid- to late Pleistocene geomorphic surfaces related to mass movement deposits (Fig. 2a, SI Appendix,

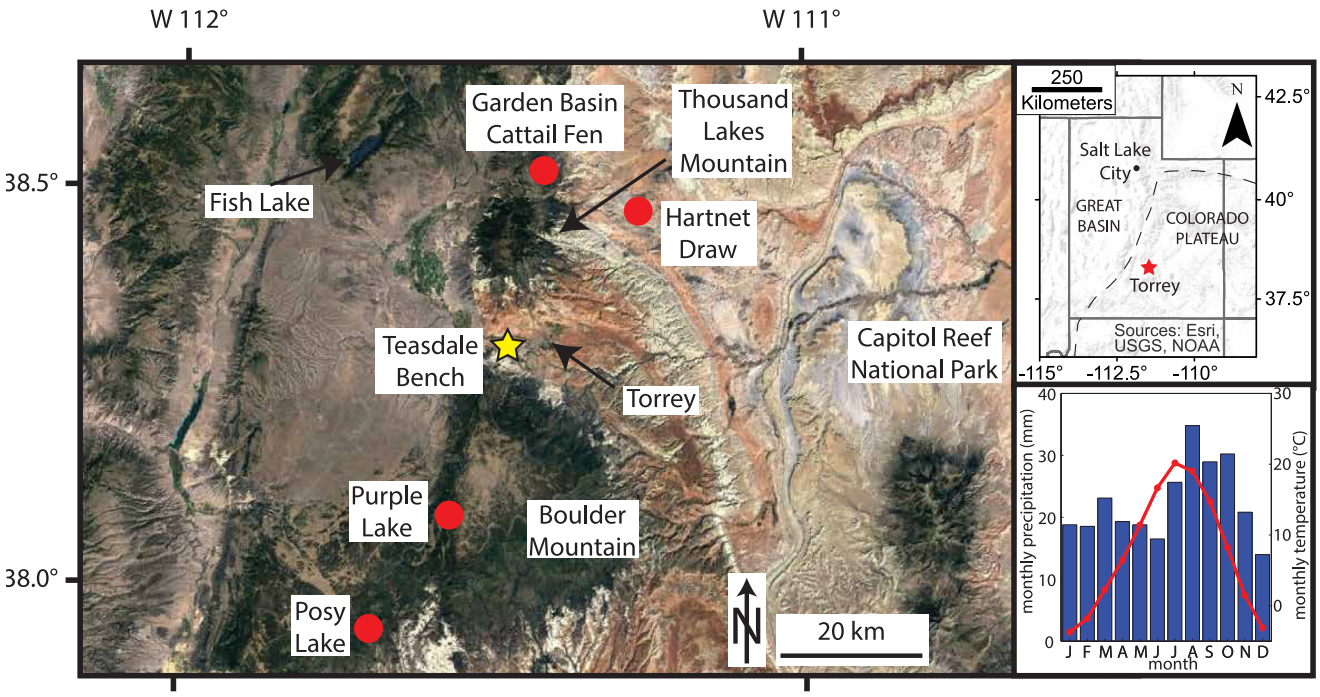

Fig. 1. Overview of the Capitol Reef region showing rind collection site (yellow star), local paleoclimate record locations (red dots), and nearby geographic points. Inset to top right shows a topographic map of Utah with a dashed line approximating the limit of the Colorado Plateau and a star denoting Torrey. See SI Appendix, Fig. S1 for a close–up of the Torrey region. Inset to bottom right shows Torrey region interpolated PRISM 30 year climate normal with precipitation (blue bar graph) and temperature (red line). Image is from Google Earth Pro. (For interpretation of the references to colour in this figure legend, the reader is referred to the web version of this article.)

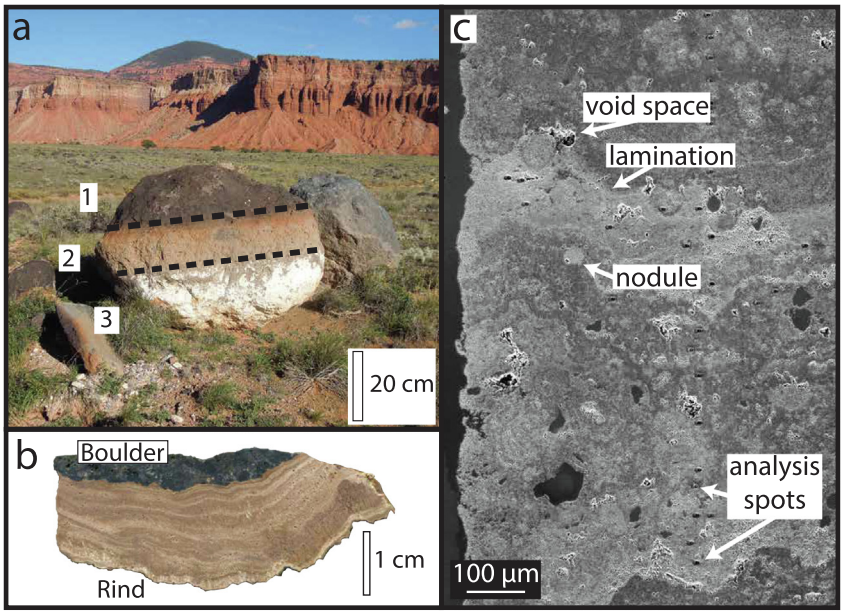

Fig. 2. Carbonate rind overview. (a) Boulder overturned during road construction at Teasdale Junction, near Torrey, Utah. Boulder surface color indicates soil horizons from when the boulder was in the ground; 1 – exposed boulder surface, 2 – Ca^{2+} leaching zone, and 3 – calcite accumulation zone (Huth et al., 2019). (b) Cross section of Pendant 11–8 that formed on the bottom of a boulder. (c) SEM secondary electron image showing rind structure and SIMS analysis spots.

Fig. S1) (Marchetti and Cerling, 2005; Marchetti et al., 2005). The surfaces are primarily composed of large (0.2 to > 1 m) trachyandesite boulders within a finer-grained matrix of mixed sedimentary units (mudstone, limestone, sands, silts, chert pebbles, etc.). This study takes place on the Teasdale Bench, which is 2100 m above sea level (masl; TB – N 38.302°, W 111.478°; SI Appendix, Fig. S1). Soils in this region have accumulated dust through time and have significant calcite accumulation consistent with local climate (≥Stage III carbonate morphology; SI Appendix, Fig. S1; Huth et al., 2019; Gile et al., 1996; McFadden, 2013). The laminated rinds of this study formed on the bottoms of large (1 m b-axis) boulders and had an identifiable stratigraphy useful for dating (Fig. 2a and b; Huth et al., 2019). Because large boulders often show surface coloration associated with *in situ* soil horizons (Fig. 2a), we could constrain the depth of formation for rinds examined in this study to > 40 cm by only collecting rinds from the largest boulders (Huth et al., 2019). Knowledge of the depth of rind formation is important, because soil carbonate formed at this depth is unlikely to have a significant influence from atmospheric CO_2, meaning that the $\delta^{13}C_{sc}$ will primarily reflect changes due to vegetation type (Cerling, 1984). Additionally, targeting large boulders for sampling ensured that rinds formed in a stable position and were not exhumed during rind formation. As only about one in thirty pedogenic rinds appeared suitable for dating (i.e., had visually continuous stratigraphy) and rinds on the bottoms of ≈1 m boulders can only be accessed *in situ* with a backhoe, we necessarily collected rinds from boulders that were excavated during highway construction on the Teasdale Bench. The selected rind, Pendant 11–8, was chosen because of its continuous stratigraphy and few large void spaces. All analyses were performed on different pieces of this rind (Fig. 2, SI Appendix, Fig. S2).

2.2. Modern soil environment and the timing of soil carbonate formation

Cycles of temperature and precipitation at Torrey cause changes in the soil environment and its associated C- and O-isotopes. In turn, the changes in soil environment control the timing of soil carbonate formation and its isotope ratios. Soil carbonate formation seasonality is therefore an important consideration in interpreting isotopic variability and we previously investigated the modern soil environment of this region as a prelude to this study (Huth et al., 2019). As a guide to readers, we describe the soil environment at 40 cm depth as analogous to the depth of rind formation (Fig. 3).

The modern soil at Torrey exhibited annual changes in soil CO_2, temperature, and moisture (Fig. 3). Soil CO_2 followed a roughly sinusoidal pattern and was lowest in winter (1000 ppm) and highest in summer (3000 to 8000 ppm). Soil temperature also exhibited a roughly sinusoidal pattern and was lowest in winter (0 °C) and highest in summer (25 °C). The timing of soil moisture changes was consistent with infiltration during snowmelt events (late winter-early spring) and during large rain events during the mid- to late summer (Huth et al., 2019).

In conjunction with these soil environment changes, the values of $\delta^{13}C_{soil-respiration}$, $\delta^{18}O_{rain}$, $\delta^{18}O_{snow}$, and $\delta^{18}O_{soil-water}$ also varied (Fig. 3a and b). The $\delta^{13}C$ of soil respired CO_2 varied in phase with soil CO_2 concentration, exhibiting

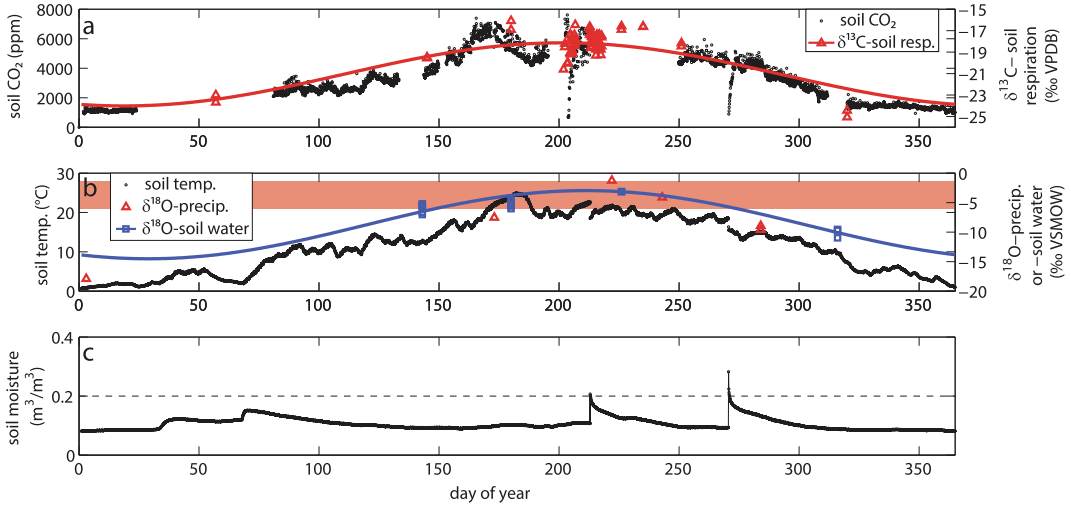

Fig. 3. Modern soil data from the study region compiled as day of year (DOY). All data were collected between 35 and 45 cm depth unless otherwise noted. (a) Soil CO_2 (black dots) and $\delta^{13}C_{soil-respiration}$ (red triangles). Red line is a sinusoidal fit to the $\delta^{13}C_{soil-respiration}$ data. The sharp decreases in soil CO_2 near days 205 and 270 (July and September) may be an instrumental artifact due to intense rainfall. (b) Soil temperature (black dots), $\delta^{18}O_{precipitation}$ (red triangles), and $\delta^{18}O_{soil-water}$ (blue squares). Blue line is a sinusoidal fit to the $\delta^{18}O_{soil-water}$ data. The red bar represents the average Holocene temperature of soil carbonate formation derived from Δ_{47} analyses (Huth et al., 2019). The $\delta^{18}O_{soil-water}$ data represent samples from 35–100 cm depth. (c) Soil moisture. Note soil isotope data were collected during different years from the environmental data and thus should only be interpreted in terms of general seasonal trends (2015–2017 and 2014–2015, respectively). See (Huth et al., 2019) for details and original dataset.

C_3-like values in the winter (-25 ‰ VPDB) and values consistent with mixed C_3–C_4 respiration in the summer (-21 to −16 ‰ VPDB). Average monthly values of $\delta^{18}O_{rain}$ and $\delta^{18}O_{snow}$ varied from −18 ‰ VSMOW in the winter to −5 ‰ VSMOW in the summer. However, $\delta^{18}O_{soil-water}$ showed more muted changes, ranging from ≤ -11 ‰ VSMOW in the winter to > -6 ‰ VSMOW in the summer (note few data points are available). Isotopic evidence of evaporation was found at all investigated soil depths, but was most prominent in summer (Huth et al., 2019).

To complement these modern observations, we also used "clumped" isotope analyses (Δ_{47}) to estimate the Holocene temperature of soil carbonate formation [$T(\Delta_{47})$] (Eiler, 2007; Ghosh et al., 2006). The estimated temperature of mineral formation, 25 °C (95% CI range 21–28 °C), unambiguously identified a summer bias in soil carbonate formation (Fig. 3b).

Given these data, we concluded that soil carbonate dominantly formed during the summer at the time of maximum annual soil moisture and soil CO_2 concentration (Huth et al., 2019). Formation was largely driven by wet-dry cycles (i.e., infiltration followed by evapotranspiration). While the timing and conditions of soil carbonate formation are clear for the modern setting, the potential exists for soil carbonate formation during other parts of the year, notably in late winter-spring during snowmelt. Therefore, a paleorecord developed at this site requires formation seasonality to be assessed through time in order for viable interpretation.

2.3. Paleorecord and age model construction

The methodology for quantitatively reconstructing $\delta^{18}O_{soil-water}$ and vegetation composition requires coupling modern soil observations, $\delta^{13}C_{sc}$ and $\delta^{18}O_{sc}$ records, and paleotemperature estimates. To that end, the record presented here is composed of radiocarbon dates, two SIMS–based $\delta^{13}C_{sc}$ and $\delta^{18}O_{sc}$ transects, three laser ablation–based $\delta^{13}C_{sc}$ and $\delta^{18}O_{sc}$ transects, and a $T(\Delta_{47})$ transect. Due to the large amount of material required for the radiocarbon and Δ_{47} analyses, we cut several slabs from Pendant 11–8 and then chose two to sample from based on their size and the visual continuity of laminations. One slab was used to acquire radiocarbon dates, laser ablation analyses, and the $T(\Delta_{47})$ transect (Fig. 4a, SI Appendix, Figs. S2 and S4) while the other slab was used for the SIMS analyses (Fig. 4b, SI Appendix, Fig. S3). We developed a single age model for the rind based on stratigraphic correlation between the two slabs and assessed its validity by comparing the overall data patterns obtained from the laser and SIMS isotope transects.

2.3.1. Sample resolution considerations

Scanning Electron Microscope (SEM) images of Pendant 11–8 showed significant fine-scale heterogeneity in lamination curvature (over 10 s–100 s µm) and, among other structures like silicate grains and void spaces, the presence of 10–100 s µm diameter carbonate nodules (Fig. 2c). The radiocarbon and Δ_{47} samples were acquired using a MicroMill system and consisted of 300–1200 µm thick sections of rind. Given the large size of these samples, it is unlikely that fine-scale lamination curvature could significantly bias the data. However, samples would have necessarily incorporated (potentially old) nodules and any reprecipitated/detrital carbonate material. Either of these sources would bias our age model and could affect paleothermometry estimates. Below, we argue against significant contribution from these errors by comparison to other paleorecords and modern soil temperature cycling. For the $\delta^{13}C_{sc}$ and $\delta^{18}O_{sc}$ profiles, we used SIMS to avoid significant time-averaging of the signal (see also SI Appendix). Given the fine analysis spot diameter for SIMS (10 µm for $\delta^{18}O$ and 7 µm for $\delta^{13}C$), we were able to avoid nodules during analysis (Fig. 2c and 4b).

2.3.2. SIMS carbon and oxygen isotope analyses

We measured $\delta^{13}C_{sc}$ and $\delta^{18}O_{sc}$ values at the University of Wisconsin–Madison WiscSIMS facility (Valley and Kita, 2009; WiscSIMS, 2020; Oerter et al., 2016). We cut two sections of Pendant 11–8 (each with dimensions of ≈0.4 × 0.7 × 1.7 cm; Fig. 4b, SI Appendix, Fig. S3) and cast them into a 25 mm diameter epoxy round mount (Buehler Epo–Thin) along with three grains of UWC–3 calcite standard ($\delta^{18}O = -17.07$ ‰ VPDB, $\delta^{13}C = -0.91$ ‰ VPDB) (Kozdon et al., 2009). After polishing, the round was sputter–coated with Au to an ≈60 nm thickness. We identified target transect sites using an optical microscope and with the University of Utah Nanofab Lab's FEI Quanta 600F Scanning Electron Microscope at 1000× magnification in secondary electron mode. We analyzed two transects (T1 and T2) for $\delta^{18}O$ and $\delta^{13}C$ using the large–radius, multicollector CAMECA IMS 1280 at WiscSIMS following previous studies (Valley and Kita, 2009; Kita et al., 2009; Williford et al., 2013). The primary beam ablated 10 µm ($\delta^{18}O$) or 7 µm ($\delta^{13}C$) diameter pits to a depth of ≈1 µm. The spot–to–spot reproducibility values for the data were determined for the eight UWC–3 standard analyses that bracketed 10–15 sample analyses; average reproducibility was ±0.2 ‰ (2 SD) for $\delta^{18}O$ and ±0.8 ‰ for $\delta^{13}C$. We defined suitable analysis spots by yield (e.g., $\delta^{13}C$ analyses with high relative yield compared to carbonate standards suggest analysis of organic carbon and should therefore be excluded; Tukey, 1977) and pit quality (e.g., pit shape, presence of cracks and inclusions; SI Appendix, Fig. S5; Wycech et al., 2018). In addition, we corrected for Mg content via Electron Microprobe Analysis (Valley and Kita, 2009; Turnier et al., 2020).

2.3.3. Clumped isotope analyses

We micromilled subsamples of soil carbonate from Pendant 11–8 in 400 µm lines at the University of Utah (Fig. 4; SI Appendix, Fig. S2). After combining one to three subsamples to acquire appropriate sample size (400–1200 µm sections for 8–10 mg per replicate), we analyzed samples and standards for Δ_{47} on an automated CO_2 extraction and purification system connected to a ThermoFinnigan MAT 253. We also made sub–daily measurements of CO_2 gases with known $\delta^{13}C$ and $\delta^{18}O$ values equilibrated at 0 °C and 1000 °C to observe instrument linearity and to generate an empirical transfer function, which allows for

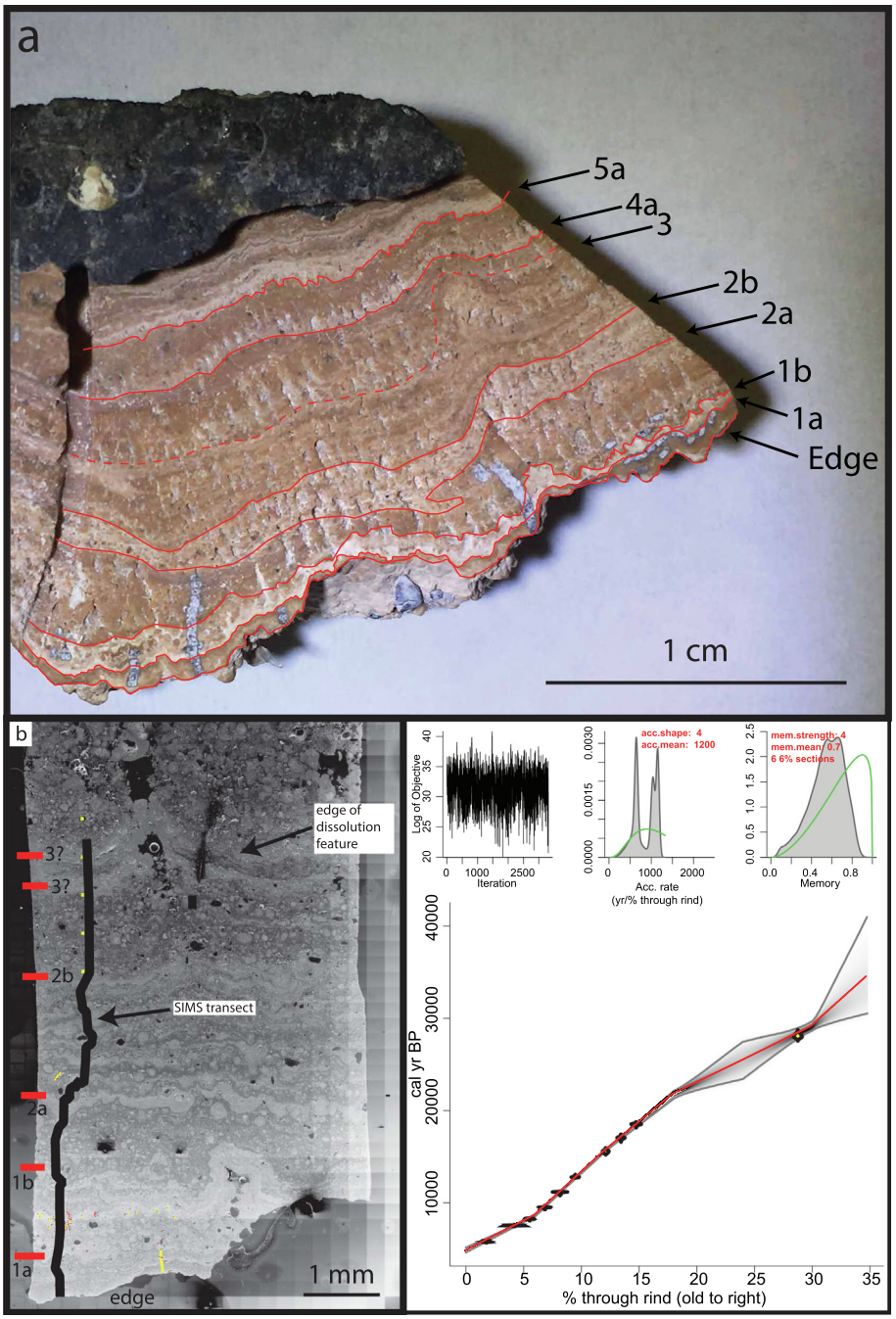

Fig. 4. Age model considerations. (a and b) Age model construction. Marker layers in the (a) milled slab of Pendant 11–8 and (b) the SIMS mount for Transect 1. Marker layers are outlined in (a) and shown on the left edge in (b). The thick black line in (b) follows the transect of SIMS analysis spots used in this study (individual spots are not visible at this scale, see also Fig. 2). The transect varies from a straight line where we avoided nodules or had to analyze several locations to acquire a suitable analysis. (c) The radiocarbon age model for Pendant 11–8 from the Bacon age-modelling program (Blaauw and Christen, 2011). The model uses "% through rind" to normalize for variable thickness along individual transects (see *section 2. Study setting and methodology*). Upper panels depict the distribution of Markov Chain Monte Carlo (MCMC) iterations (left panel), and the prior (green curves) and posterior (grey histograms) distributions for the accumulation rate (middle panel) and memory (right panel). Bottom panel shows the age model. Yellow shapes with thick black outlines are contours of calibrated radiocarbon dates (size is exaggerated for visibility). Darker shading indicates more likely calendar ages along the age model, gray curves are the 95% confidence intervals, and red curve is the "best" model based on the mean age for each depth. See also SI Appendix, Tables S3–S5 and Figs. S2–S4 for additional information.

presenting data in an absolute reference frame (Dennis et al., 2011). Data were corrected for mass interference from ^{17}O (Schauer et al., 2016; Kelson et al., 2020). For reference, we observed the following Δ_{47} values for carbonate standards analyzed during the same analytical session: NBS-19, 0.389 ± 0.013 ‰ (1 s, $n = 21$); HAF Carrara

(a.k.a. YCM), 0.383 ± 0.012 ‰ (n = 19); 102-GC-AZ01, 0.692 ± 0.013 ‰ (n = 36).

2.3.4. Radiocarbon dating

We milled sections from the rind (Pendant 11–8) to obtain approximately 10 mg of sample (SI Appendix, Fig. S2). We extracted CO_2 from samples, purified the gas under vacuum, and graphitized it before AMS (accelerator mass spectrometry) and $\delta^{13}C$ measurements at the Arizona AMS Laboratory. Samples labeled 14C-2016–0## (where "##" is a unique sample number) are from a single transect and were acquired by combining several sub–samples, milled at 100 μm resolution (generally 300 μm sections; see sub-sample milling information in SI Appendix, Fig. S2, Table S5). In an attempt to extend the age model past 18 ka, samples TR-04 and TR-05 were milled from the same slab, but on a different transect ≈1 cm away from the 14C-2016–0## samples. To minimize the width of sampling footprint and allow the same slab to be used for all radiocarbon samples, TR-0# samples were acquired by (1) milling single sections following the diameter of the drill bit and then (2) chipping out the material outlined by the milled sections (SI Appendix, Fig. S2). For age model construction, distance–age correlation was based on distance along the rind for the transect of 14C–2016–0## samples, with TR–0# samples transposed to this transect by following prominent laminations that guided drilling. Their reported boundary and midpoint positions therefore have higher uncertainty than other samples (SI Appendix, Table S5), but the exact positions picked do not affect our interpretation. A dissolution feature identified in the sample constrains the upper age limit of the transect (SI Appendix, Figs. S2 and S3) and we exclude TR-05 from the age model as it may have incorporated some of this material.

2.3.5. Age models for clumped isotope and SIMS data

We constructed the age model using the Bacon age-modeling software, which utilizes IntCal13 to calculate calibrated radiocarbon ages (Fig. 4; Blaauw and Christen, 2011; Reimer et al., 2013). Radiocarbon samples track the average growth rate of the rind. However, different rind locations had variable growth rate compared to the average rind growth rate (e.g., compare slabs in Fig. 2b, 3a, SI Appendix, Figs. S2–S3), which is especially important to assess for SIMS transects considering the fine scale of analysis (<10 μm spots). To account for this variability along individual transects, the age model for the SIMS data was based on linear interpolation between marker laminations that was then tied to the Bacon age model. As a result we use the metric "% through rind" for our age model (Fig. 4c), which can be converted to true distance (i.e., mm from rind edge) for any piece of rind by measuring the distance between marker laminations and the total rind thickness at that point (Fig. 2b, SI Appendix, Fig. S3, Table S5). Marker laminations for the youngest material (<11 ka) were unambiguous but older marker laminations were not as clear, so we have most confidence in the timing of changes observed for the Holocene. Each SIMS transect was fit with a 1000-yr window moving average to highlight temporal trends.

In addition to our observation that the two slabs share marker laminations, we justify our age model by comparing stable isotope transects between the two. We used a laser ablation GC/IRMS system (method of Passey and Cerling, 2006) on the same slab used for ^{14}C and Δ_{47} sampling to quickly acquire three coarse-resolution isotope transects, with each analysis composed of 2–100 μm diameter spots. Data was standardized to a single in-house calcite standard (Laser Marble Std; $\delta^{18}O = -4.80$ ‰ VPDB, $\delta^{13}C = 1.37$ ‰ VPDB) and blank determinations were negligible so we did not apply a blank correction (Passey and Cerling, 2006). Like the SIMS data, the age model for the laser ablation data was based on linear interpolation between marker laminations that was then tied to the Bacon age model. We expected SIMS- and laser ablation-derived data to be offset from one another because of their different standardization routines. In addition, we expected that the coarser spatial resolution of the laser ablation analyses would tend to mute observed isotopic variability as compared to the SIMS data. Even with these constraints, laser ablation-derived and SIMS-derived data largely show the same isotopic patterns, supporting our age model (SI Appendix, Fig. S4). We do not interpret the laser ablation-derived transect further, given the coarse resolution of the analyses compared to the SIMS analyses.

In order to highlight temporal trends in $T(\Delta_{47})$, especially where data have single replicates (26–6 ka), we took weighted averages of the data over the following intervals: 0–10, 10–15, 15–20, 20–25, and 25–35 ka. We calculated $T(\Delta_{47})$ using the inorganic calibration of (Defliese et al., 2015) and provide ranges for one standard error of the mean (SE) and the 95% confidence interval (95% CI) (Fig. 5). Our interpretation is insensitive to choice of calibration and intervals (SI Appendix, Fig. S6, Table S1; Bonifacie et al., 2017; Henkes et al., 2013).

2.4. Paleoenvironmental reconstruction methodology

2.4.1. Vegetation composition reconstruction

We modeled vegetation composition as the percentage of C_3 plants active on the landscape at the time of mineral formation (%C_3–plants; Fig. 6; SI Appendix, Figs. S7 and S8) Forward models exist to predict $\delta^{13}C_{sc}$ from observed $\delta^{13}C_{soil-CO2}$ (Cerling, 1984; Davidson, 1995). We used a Monte Carlo approach that combined our knowledge of past environmental conditions in conjunction with the model of (Davidson, 1995) to quantitatively reconstruct past vegetation composition. The process involves three steps: (1) using the range of late Quaternary environmental conditions to model all possible values of $\delta^{13}C_{sc}$, (2) determining the plausible conditions of soil carbonate formation by comparing modeled environmental conditions with known soil conditions, and (3) converting the plausible values of $\delta^{13}C_{soil-respiration}$ to %C_3–plants on the landscape.

We first created a set of all values of $\delta^{13}C_{sc}$ possible under late Quaternary climate conditions. These model values serve as potential matches for the observed data in the second step, where we invert for $\delta^{13}C_{soil-respiration}$. To create the possible Quaternary values, we modeled $\delta^{13}C_{soil-CO2}$ and then converted it to $\delta^{13}C_{sc}$. We modeled $\delta^{13}C_{soil-CO2}$

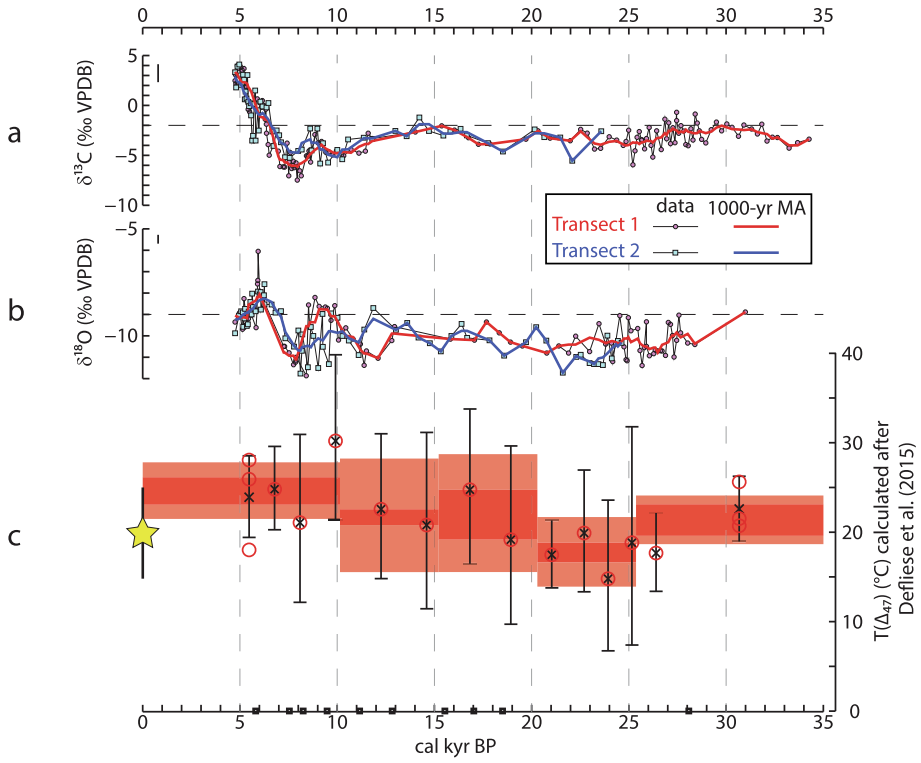

Fig. 5. Laminated soil carbonate isotope records. (a) Soil carbonate $\delta^{13}C$ and (b) $\delta^{18}O$ records from SIMS, this study. Red and blue symbols are two transects from Pendant 11–8 (average ± 2 SD precision of ±0.2 ‰ for $\delta^{18}O$ and ±0.8 ‰ for $\delta^{13}C$ are short vertical lines in the upper left corners) and thick lines are 1000–yr window moving averages (1000–yr MA). Radiocarbon dates are black squares at the bottom. (c) Formation temperature estimates (Defliese et al., 2015) through time for this study showing individual measurements (red circles), sample averages (black x's, note not all samples have replicates), and sample 95% confidence intervals. Horizontal bars show 1 standard error (dark red) and the 95% confidence interval (light pink) for data within an interval (see text for details). Modern JJAS average, minimum, and maximum soil temperature are shown by the yellow star with black lines, respectively (data for years 2014–2015 from Huth et al., 2019).

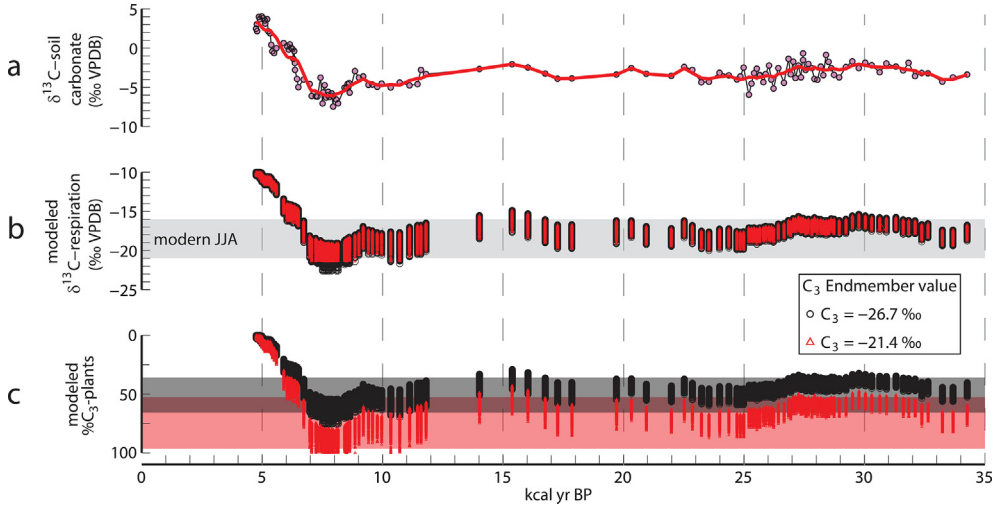

Fig. 6. Paleovegetation reconstruction at Torrey, UT. Only Transect 1 is shown for clarity (see Transect 2 in SI Appendix, Fig. S7). (a) $\delta^{13}C_{sc}$ as in Fig. 5. (b) Modeled $\delta^{13}C_{soil-respiration}$ with gray bar representing modern observed range during June-August. (c) Modeled $\%C_3$–plants for two different C_3 endmembers (red triangles = −21.4 ‰ VPDB; black circles = −26.7 ‰ VPDB). Both scenarios use a C_4 endmember of −10 ‰ VPDB and are constrained by soil $CO_2 \geq 1000$ ppm. The overlapping red and gray bands correspond to the two endmember scenarios and show the modern observed range during June-August transposed into $\%C_3$–plants. Note the inverted y–axis in (c).

using a steady-state system with two CO_2 sources (soil respiration and air) and dominated by diffusive transport (Davidson, 1995). The model uses inputs of soil CO_2 concentration, $\delta^{13}C_{soil-respiration}$, atmospheric CO_2 concentration, and $\delta^{13}C_{atmospheric-CO2}$. We ran 10^7 simulations over a range of values representative of all possible late Quaternary conditions; in other words the entire range of $\delta^{13}C_{soil-respiration}$ values possible with C_3 and C_4 photosynthesis was included and soil CO_2 was allowed to be as low as atmospheric levels (soil $CO_2 = 150$–10,000 ppm, $\delta^{13}C_{soil-respiration} = -10$ to -30‰ VPDB, atmosphere $CO_2 = 150$–300 ppm, and $\delta^{13}C_{atmospheric-CO2} = -6$ to -7‰ VPDB). We converted the modeled $\delta^{13}C_{soil-CO2}$ values to $\delta^{13}C_{sc}$ using our paleothermometry estimates in conjunction with a temperature-dependent fractionation factor over the range 10–30 °C (Romanek et al., 1992).

Second, we determined the model conditions that could plausibly create the moving average $\delta^{13}C_{sc}$ values in order to infer the $\delta^{13}C_{soil-respiration}$ at the time of sample formation; in other words, we inverted for $\delta^{13}C_{soil-respiration}$ using reasonable constraints on variables. This was done by comparing $\delta^{13}C_{sc}$, soil temperature, atmospheric CO_2 concentration, and soil CO_2 concentration of modeled conditions and measured or inferred past conditions. We used our isotopic analyses to constrain $\delta^{13}C_{sc}$ and soil temperature. We required modeled values of $\delta^{13}C$ to be within ±0.1‰ of the moving average $\delta^{13}C$ values. For temperature, each moving average-filtered $\delta^{13}C_{sc}$ datum was assigned a paleotemperature range (SE and 95% CI) based on its age. Modeled soil temperature was required to be within this range.

Atmospheric CO_2 concentration and its $\delta^{13}C$ were matched to gas measurements from polar ice cores within a 500 yr age window (Eggleston et al., 2016; [dataset] Bereiter et al., 2015). This allowed each datum to be matched to at least one set of atmospheric values. A minimum level of variability was set around the mean of all data points that allowed the simulation to proceed in a reasonable number of runs, but that would not significantly influence the results (±5 ppm for atmospheric CO_2 and ± 0.1 ‰ for $\delta^{13}C_{atmospheric-CO2}$).

For soil CO_2, constraining its lower boundary was especially important because atmospheric CO_2 is an important contributor to soil CO_2 under near-atmospheric soil CO_2 levels. If soil CO_2 concentration is low, $\delta^{13}C_{soil-respiration}$ is difficult to determine because respiration contributes relatively little to the overall soil CO_2 pool (note that for a set respiration rate, this effect is diminished under lower atmospheric pCO_2 conditions like those of the Last Glacial Maximum). Modern soil carbonate at Torrey forms in summer when annual soil CO_2 is at its highest (3000–8000 ppm) and modern soil CO_2 never drops below 1000 ppm in winter (Fig. 3; Huth et al., 2019). In addition, our paleothermometry data demonstrate consistent summer formation throughout the record (see *3. Results*). Given these constraints, and even considering a 50% decrease in summer soil CO_2, we argue it is likely that soil CO_2 was always several times atmospheric levels during soil carbonate formation. We therefore used soil $CO_2 = 1000$–8000 ppm to select plausible scenarios for the data set.

Once the plausible scenarios had been identified, we quantified vegetation composition for each data point by converting model values of $\delta^{13}C_{soil-respiration}$ to $\%C_3$–plants. This conversion was made using a two-endmember mixing model under the assumption that $\delta^{13}C_{soil-respiration}$, and thus $\delta^{13}C_{sc}$, is largely derived from near-contemporaneous plant material. Choice of the C_3 and C_4 endmember values was important because the difference between $\delta^{13}C_{plant}$ and $\delta^{13}C_{atmospheric-CO2}$ (the source signal for plants) can also be a function of other variables (Ehleringer and Monson, 1993; Breecker et al., 2012a). The value of the C_3 endmember may be estimated, in conjunction with known pCO_2 and $\delta^{13}C_{atmospheric-CO2}$ conditions, as a function of water stress or atmospheric CO_2 concentration (e.g., Schubert and Jahren, 2012; Schubert and Jahren, 2018; Breecker, 2017; Hare et al., 2018; Diefendorf et al., 2010; Kohn, 2010; Kohn, 2016; Bowling et al., 2002), so we allowed a range of values based on these calibrations.

For the CO_2 concentration effect, we considered the multiple species calibration of Schubert and Jahren (2012; their Eq. 6), which can be applied to each data point based on the CO_2 concentration and $\delta^{13}C_{atmospheric-CO2}$ conditions inferred from ice core records. The calculated $\delta^{13}C$ range of the C_3 endmember as a function of atmospheric CO_2 concentration was –25.6 to –22.9 ‰ VPDB (SI Appendix, Fig. S8).

For the water stress effect, we considered the calibrations of Diefendorf et al. (2010) and Kohn (2010). Both calibrations are primarily functions of mean annual precipitation (MAP), but also utilize secondary parameters. We followed the authors' apparent or stated preferred calibrations; Diefendorf et al. (2010) also consider altitude (global relationship in their Supporting Information, pg. 3) and Kohn (2010) also considers altitude and latitude (their Eqn. 2). We considered an MAP range of 130–1040 mm/yr (i.e., 0.5–4 × modern MAP) as likely to cover that experienced at Torrey, UT over 0–35 ka (e.g., Marchetti et al., 2011; Oster et al., 2015; Anderson et al., 2000). This range also uses modern elevation-climate relationships as an analog for Last Glacial Maximum (LGM, 25–20 ka) climate. During the LGM, plants had elevational depressions of 100 s–1000 m below present day locations (Anderson et al., 2000). Modern MAP in the highlands near Torrey, which are 800–1000 m higher, have MAP ranges of 600–900 mm/yr and mean annual temperature values that are ≥ 7 °C cooler (Horel et al., 2020; Prism Climate Group, 2018). While a simple elevation-based translation of modern climate is not a perfect analog, we use it as a reasonable estimate of the magnitude of change in lieu of past MAP estimates. As with the CO_2 concentration calibration, we included the range of $\delta^{13}C_{atmospheric-CO2}$ conditions inferred from ice core records over 0–35 ka. The calculated $\delta^{13}C$ range of the C_3 endmember as a function of MAP was –26.7 to −21.4 ‰ VPDB (SI Appendix, Fig. S8).

Combined, these two calibrations give an overall $\delta^{13}C$ range for the C_3 endmember of –26.7 to −21.4 ‰ VPDB (see SI Appendix, Fig. S8 for plots using individual calibrations). We set the $\delta^{13}C$ value for the C_4 endmember to −10 ‰ VPDB based on the average isotopic compositions of pre-industrial plants following the C_4 photosynthetic

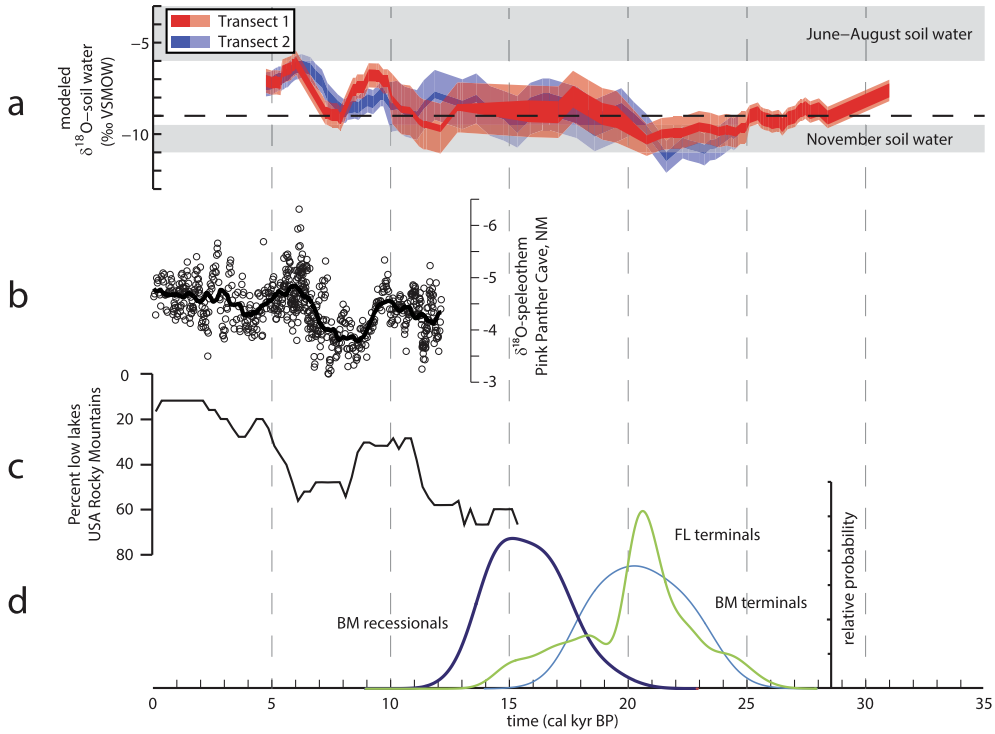

Fig. 7. Reconstructed $\delta^{18}O_{soil-water}$ and regional proxy comparison. (a) Modeled $\delta^{18}O_{soil-water}$ (this study). Transect colors and temperature intervals are as in Fig. 5, with the darker fill calculated from the temperature estimate standard error and the lighter fill calculated from the 95% confidence interval. Gray bars show the range of values for modern soil water in November and June-August, respectively (Fig. 3). (b) Record of $\delta^{18}O_{calcite}$ for a speleothem from Pink Panther Cave, New Mexico (≈900 km to the southeast; Asmerom et al., 2007). Black line is a 1000–yr window moving average. (c) Compilation of when USA Rocky Mountain lakes were anomalously low (Schuman and Serravezza, 2017). (d) Terminal and recessional moraines from the Last Glacial Maximum and the late Pinedale on Boulder Mountain (BM) and Fish Lake (FL), which is on Fish Lake Mountain (Marchetti et al., 2005; Marchetti et al., 2011) (Fig. 1). Note the inverted y–axes in (b) and (c).

pathways and the effects of water stress on plant $\delta^{13}C$ values (Cerling and Harris, 1999; Tipple and Pagani, 2007).

2.4.2. Reconstruction of soil water oxygen isotope composition ($\delta^{18}O_{soil-water}$)

The distribution of isotopes between two phases in equilibrium, here soil carbonate and soil water, can be described by a temperature-dependent fractionation factor. We thus modeled $\delta^{18}O_{soil-water}$ by using the moving average-filtered $\delta^{18}O_{sc}$ profiles and paleothermometry estimates (Fig. 7). We assigned each $\delta^{18}O_{sc}$ datum a paleotemperature range (SE and 95% CI) based on its age. The relevant temperature-dependent fractionation factors were calculated for each point (Kim and O'Neil, 1997) and used to model the range of $\delta^{18}O_{soil-water}$ values consistent with the data. Other calibrations for the fractionation factor are possible (Coplen, 2007; Affek and Zaarur, 2014), but note that the similar temperature sensitivity of all three calibrations necessarily produces similar patterns of reconstructed $\delta^{18}O_{soil-water}$ (SI Appendix, Fig. S9). However, use of the Coplen (2007) calibration will shift data more negative by ≈1.5 ‰ and use of the Affek and Zaarur (2014) calibration will shift data more negative by < 1 ‰ and result in more muted patterns due to a smaller temperature sensitivity than the other calibrations. Therefore, while we present the reconstruction using the Kim and O'Neil (1997) calibration, we emphasize that patterns of change are the most robust aspect of the $\delta^{18}O_{soil-water}$ reconstruction. Beyond calibration choice, the large 5–10 ka intervals used to average T(Δ_{47}) are the biggest source of error in our approach. This error can likely be minimized by finer spatial sampling enabled by smaller analysis size than was available at the time of this study (≈10 mg/replicate vs. < 3 mg/replicate).

3. RESULTS

3.1. Age model and paleothermometry

Calibrated radiocarbon dates for Pendant 11–8 were in stratigraphic order and the age model spanned 35–5 ka (Fig. 4). Reconstructed soil temperatures during rind formation were ≈18 °C during the Last Glacial Maximum and 20–25 °C at other times (Fig. 5c).

3.2. Rind carbon isotope composition and vegetation composition reconstruction

The $\delta^{13}C_{sc}$ transects spanned 35–5 ka and largely agree in pattern (Fig. 5a). From 35–10 ka, $\delta^{13}C_{sc}$ was fairly con-

stant between −2 to −4 ‰ VPDB. However, during the Holocene it spanned a large, 10 ‰ range. Values of $\delta^{13}C_{sc}$ data were lower from 9–7 ka at −4 to −6 ‰ VPDB, and starting at 7 ka they increased towards the present until they reached their highest values, +3 ‰ VPDB, at 5 ka.

Reconstructed vegetation composition follows these same trends, with the highest inferred $\%C_3$–plants corresponding to the lowest $\delta^{13}C_{sc}$ values (Fig. 6). Reconstructed vegetation ranged from 0–100 $\%C_3$–plants for the −21.4 ‰ VPDB endmember and 0–75 $\%C_3$–plants for the −26.7 ‰ VPDB endmember. During the last glacial period, the vegetation generally consisted of 30–90 $\%C_3$–plants, which increased to a maximum of 45–100 $\%C_3$–plants during the Early Holocene. This was followed by a large decline in C_3 plants starting at 7 ka. By 3 ka, we model 0–10 $\%C_3$–plants on the landscape.

3.3. Oxygen isotope composition of rind and reconstructed soil water

The $\delta^{18}O_{sc}$ transects show the same general patterns, but significant discrepancies between the transects exist, notably from 12–8 ka (Fig. 5b). Discrepancies are potentially derived from issues with the age model, difficulty obtaining suitable analysis spots, data density (especially > 15 ka), and/or small scale variability in $\delta^{18}O_{soil-water}$ at the time of mineral formation (e.g., Gazis and Feng, 2004; Treadwell-Steitz and McFadden, 2000; Sprenger et al., 2016). From 31–9 ka, $\delta^{18}O_{sc}$ ranged from −9 to −12 ‰ VPDB where analysis spots were most concentrated. The transects differ by up to 1.5 ‰ from 12–10 ka, although note the limited analysis spots in this time slice. Transect 1 increases from −11 to −9 ‰ VPDB between 11–9 ka and then decreases to −11 ‰ VPDB by 8 ka. Transect 2 may show a similar trend, but identifying trends at this time is difficult because it is not clear if the variability between successive data points is real or an issue with the age model or obtaining suitable SIMS analysis spots (e.g., relative yield or pit quality were poor; see also SI Appendix, Fig. S5). The transects show good agreement for the remainder of the record. From 8–6 ka, both transects increase to −8 ‰ VPDB and then decrease slightly to −9 ‰ VPDB at the end of the record.

Reconstructed $\delta^{18}O_{soil-water}$ ranged from −11 to −6 ‰ VSMOW, varying between the full range of modern observed $\delta^{18}O_{soil-water}$ values (Fig. 7). The largest difference in pattern between $\delta^{18}O_{soil-water}$ and $\delta^{18}O_{sc}$ is at 25–20 ka. Between 25–20 ka, $\delta^{18}O_{soil-water}$ is −11 to −10 ‰ VSMOW, and then increases during deglaciation to −9 to −8 ‰ VSMOW. In contrast, $\delta^{18}O_{sc}$ remains fairly constant through time. This difference is driven by the change in formation temperature between 25–20 ka (Fig. 5c). At all other times, $\delta^{18}O_{soil-water}$ generally follows the same pattern as $\delta^{18}O_{sc}$. The two $\delta^{18}O_{soil-water}$ transects are in disagreement by up to 2 ‰ between 12–9 ka, but then both increase to −9 ‰ VSMOW by 8 ka. Between 8–4 ka, both transects showed $\delta^{18}O_{soil-water}$ increasing from −9 to −6 ‰ VSMOW, and then decreasing slightly to −7.5 ‰ VSMOW at the end of the record.

4. DISCUSSION

4.1. Late Quaternary climate and vegetation change in Torrey, UT

4.1.1. Soil carbonate formation conditions inferred through time

Reconstructed soil temperature over the last 40 ka most likely reflects summer soil temperature. The temperature increase from the LGM to the Holocene of ≈7 °C is consistent with previous inferences of regional change (Fig. 5). For example, Marchetti et al. (2011) used terminal and recessional moraines on the nearby Boulder and Fish Lake Mountains (dated to 23–19 ka and 16–14 ka respectively) to estimate summer temperature depression as compared to modern (Fig. 7). Our estimate of summer soil temperature depression between the Holocene and LGM is similar to or smaller than their estimates for summer temperature depression for the > 2700 m Fish Lake Plateau depending on precipitation amount (-10.7 to −8.2 °C for LGM precipitation = 1 × modern, −6.7 to −9.2 °C for LGM precipitation = 1.5 × modern; Marchetti et al., 2011).

The continuously warm soil temperature data support interpreting the $\delta^{13}C_{sc}$ and $\delta^{18}O_{sc}$ data in the context of our modern calibration study where soil carbonate forms in the warmest summer months (Fig. 3). Significant summer rainfall must have always occurred in the last 40 ka to allow soil carbonate to consistently form in the summer. A shift to a different regime of rainfall seasonality would require soil carbonate to form at a different time of year and reconstructed soil temperature would accordingly not be uniquely consistent with summer values. This validates our approach in modeling $\delta^{13}C_{sc}$ and $\delta^{18}O_{sc}$ as the $\%C_3$–plants and $\delta^{18}O_{soil-water}$, respectively, that are present during summer (as opposed to mean annual conditions). Within this framework, we note the most negative reconstructed $\delta^{18}O_{soil-water}$ values (-11 to −12 ‰ VSMOW; Fig. 7; SI Appendix, Fig. S9) are well outside the modern observed summer range; we explore explanations for this observation below.

4.1.2. Climate and vegetation composition during the last glacial period

We discern broad trends in our record during the last glacial period but we cannot address millennial-scale variability during this time period as data density and age control are imprecise. During the last glacial period model estimates generally show a mix of C_3 and C_4 plants existed on the landscape (30–90 $\%C_3$–plants Fig. 6), although note that the wide constraints on the C_3 endmember value preclude a precise estimate. However, climate during the last glacial period in the western USA was cooler and may have had increased effective moisture, as evidenced by the greater extent of lakes, glacial advances, and shifts in vegetation boundaries by latitude and elevation (Marchetti et al., 2011; Coats et al., 2008; Madsen et al., 2001; Anderson et al., 2000). This suggests that scenarios using more negative C_3 endmember values, associated with a larger C_4 plant proportion, are most likely. Our interpretation is consistent

with other regional records suggesting that C_4 plants persisted through the last glacial period (Cole and Monger, 1994; Liu et al., 1996), with the implication that climate conditions were generally suitable for C_4 plants due to lower atmospheric CO_2 concentration accompanied by warm season rainfall (Ehleringer et al., 1997).

The overall decrease in $\delta^{18}O_{soil-water}$ at the LGM and then increase during deglaciation could have been driven by changes in the air temperature during rainfall, infiltration seasonality, evaporation intensity, and/or source water (Fig. 7). The NAM may derive water from both the Gulf of Mexico and the Gulf of California, which could produce ≈1 ‰ variability in our record (Schmidt et al., 1999) and changes in winter source water could cause several per mil variability (Lachniet et al., 2014). Increasing air temperature by ≈7 °C from 25–10 ka could also have driven a substantial portion of the overall increase in $\delta^{18}O_{soil-water}$ via changes in $\delta^{18}O_{rain}$ and $\delta^{18}O_{snow}$. Likewise, as the region warmed during this time period, increasing evaporation intensity could have driven increasing $\delta^{18}O_{soil-water}$. Changing the proportion of seasonal infiltration could also cause a comparable increase in $\delta^{18}O_{soil-water}$.

While disentangling these effects is difficult in a single record, our $\delta^{18}O_{soil-water}$ data are consistent with interpretations from other climate records. Cooler temperature during meteoric precipitation events and decreased soil evaporation would both act to decrease $\delta^{18}O_{soil-water}$ values in the LGM portion of the record. Then, as temperature (and soil evaporation) increased during the deglaciation, $\delta^{18}O_{soil-water}$ values would have correspondingly increased. Increased moisture delivery or changing moisture source region during winter at the LGM is also consistent with the Torrey $\delta^{18}O_{soil-water}$ reconstruction (Oster et al., 2015; Lachniet et al., 2014).

4.1.3. Climate and vegetation composition during the Holocene

The greater data density and age control in the Holocene portion of the Torrey record allow for more detailed interpretation and record comparison. We infer that vegetation underwent a dramatic shift from the Early to Middle Holocene (Fig. 6). Between 10–7 ka, C_3 plants dominated the landscape, reaching their greatest abundance between 7 and 9 ka (45–100 $\%C_3$–plants). After this point, C_3 plants declined until they were essentially absent on the landscape by 5 ka (<10 $\%C_3$–plants). Note that $\delta^{13}C_{sc}$ at 5 ka is so positive that our interpreted decline is robust to even C_3 endmember values of −30 ‰ VPDB. As part of this interpretation, we infer that the ≈10 ‰ $\delta^{13}C_{sc}$ shift from 7–5 ka was caused by an increase in C_4 vegetation and not a decline in overall summer respiration (Cerling, 1984). Three lines of evidence support this inference. First, consistent formation of soil carbonate in the summer throughout the Holocene requires summer rainfall be an important contributor to annual rainfall (Huth et al., 2019). Second, if the highest $\delta^{13}C_{sc}$ values (+3 ‰ VPDB) were created in a mixed C_3-C_4 environment similar to modern (≈50 $\%C_3$–plants), soil respiration would have to be reduced by > 99%. Modern soil pCO_2 values consistent with such low respiration are not observed even in mid-winter at Torrey (≈1000 ppm CO_2; Fig. 3). Additionally, the required dry annual conditions would be more consistent with soil carbonate formation at the soil surface and not at 40 cm depth. Third, a local packrat midden sequence from nearby Hartnet Draw in Capitol Reef National Park (1920 masl, 25 km from Torrey; Fig. 1) supports the inference of significant respiration from vegetation growing during the summer (Cole et al., 1997). The Hartnet Draw midden sequence documented a significant grass and shrub component at 5.4 ka, which the authors interpreted as a relatively stable vegetation regime until the advent of intensive grazing in the 1800 s. However, packrat middens are, like all proxies, imperfect recorders and are thought to quantitatively underestimate the abundance of grasses on the landscape (Betancourt et al., 1990). When combined with our soil carbonate record, it is clear that while the overall landscape may have been consistently dominated by shrubs and grasses through the Mid- to Late-Holocene, significant changes in the favored plant photosynthetic pathway occurred.

We interpret the Holocene $\delta^{18}O_{soil-water}$ data in the context of the $\%C_3$–plants record (Fig. 7). In regions with summer rainfall regimes, C_4 plants generally outcompete C_3 plants under higher summer temperature (Ehleringer and Monson, 1993; Ehleringer et al., 1997; Holmgren et al., 2007; but see also, e.g., Cole and Monger, 1994); such relationships have been demonstrated over large geographic and altitudinal ranges (Ehleringer et al., 1997; Nordt et al., 2007; Teeri et al., 1980; Teeri and Stowe, 1976; Wentworth, 1983). Because these relationships have historically been developed in the context of plant abundance within a biome, they do not explicitly account for seasonal productivity. This is an important consideration in the context of the summer-biased Torrey record as temporal separation in C_3-C_4 plant activity has been documented in similar semi-arid environments (e.g., Kemp, 1983; but see also Bowling et al., 2011). We therefore stress that the Torrey paleovegetation reconstruction provides information about *summer* conditions and correspondingly may only provide a minimum estimate of mean annual $\%C_3$–plants (i.e., C_3 plant abundance within a biome). In addition, we recognize that complicating situations exist where the predicted relationship between increased temperature and the abundance of C_4 plants does not hold (e.g., Cole and Monger, 1994).

Regardless of these other effects, temperature is likely still an important control on $\%C_3$–plants and we subsequently use this relationship as one pathway to interpret the Holocene $\delta^{18}O_{soil-water}$ interpretation. In the context of the above seasonal bias considerations, the scale of temperature change required to produce large apparent $\%C_3$–plants changes (Fig. 6) should be less than required by modern continental-scale calibrations (a few degrees Celcius vs. ≈10 °C). Note that because our reconstructed temperature data have coarse temporal resolution and, in general, have few replicates, this dataset cannot be used to directly identify Holocene temperature change. Nonetheless, from the start of the Holocene to 7 ka we infer relatively cool conditions must have existed to support a summer landscape composed dominantly of C_3 plants

(Ehleringer et al., 1997). During this period of relative vegetation stability, summer $\delta^{18}O_{soil-water}$ values varied by 3 ‰. We cannot explicitly rule out changes in air temperature or evaporation intensity and their effects on $\delta^{18}O_{soil-water}$. However, if air temperature (and by association evaporation intensity) varied significantly throughout this interval, $\%C_3$–plants values should not have maintained a relatively narrow range. Changing summer source water could potentially explain ≈1 ‰ of the variability, but such changes are not inferred to occur until the Mid-Holocene (Barron et al., 2012); in any event this is not a sufficient isotopic driver. Instead, changes in winter source water (e.g., Lachniet et al., 2014) and/or the relative proportion of seasonal infiltration are more likely drivers. Each winter, snowmelt "resets" $\delta^{18}O_{soil-water}$ to a baseline value, which today is several per mil higher than $\delta^{18}O_{snow}$ (Fig. 3). Then, over the course of the summer, $\delta^{18}O_{soil-water}$ is driven to higher values as a result of summer rainfall and evaporation (Huth et al., 2019). By having more winter infiltration or infiltrating water with lower $\delta^{18}O$, the springtime baseline $\delta^{18}O_{soil-water}$ could be lowered and summer $\delta_{18}O_{soil-water}$ values could be significantly altered.

We therefore interpret the Early Holocene $\delta^{18}O_{soil-water}$ data in the context of source water and infiltration. In the earliest Holocene, increased winter infiltration or a more northerly moisture source created lower $\delta^{18}O_{soil-water}$. Then, the soil system began to receive relatively less winter infiltration, or moisture from a more southerly source, reaching a local maximum in $\delta^{18}O_{soil-water}$ values around 8 ka. Lower $\delta^{18}O_{soil-water}$ conditions were established towards 7 ka via more winter infiltration or water from a more northerly source. From 7–5 ka, C_3 plants on the landscape were replaced by C_4 vegetation (Fig. 6), suggesting increasing temperature began to play an important role in soil water cycling along with infiltration seasonality and moisture source. Increasing evaporation intensity driven by higher summer temperature may therefore have caused the increase in $\delta^{18}O_{soil-water}$ from 7–6 ka. The final recorded decrease in $\delta^{18}O_{soil-water}$ from 6–5 ka occurred as C_3 plants continued to decline. The continued decline in C_3 plants is consistent with increasingly warm summer conditions, which makes it unlikely that evaporation intensity would have lessened at this time. Instead, we infer that the decrease in $\delta^{18}O_{soil-water}$ was driven either by increased winter infiltration or a moisture source with a lower $\delta^{18}O$ value.

Paleorecords developed from lakes and wetlands near Torrey (Fig. 1) support a combination of infiltration seasonality and evaporation intensity as primary drivers of $\delta^{18}O_{soil-water}$ change but do not speak to seasonal moisture sources. On the basis of pollen ratios for plants with different hydrologic niches, the authors of these studies qualitatively inferred changes in local hydrologic processes through time. Two mid-elevation records from Garden Basin Cattail Fen (≈2400 masl) and Posy Lake (2646 masl) document high Early Holocene annual moisture decreasing between 8–7 ka and 5–4 ka, respectively, due to decreased summer moisture (Morris et al., 2013; Shurtliff et al., 2017) with increasing moisture occurring in the Late Holocene. In addition, inferred treeline elevation increased between the Early and Mid-Holocene, which suggests increasing temperature at this time. Discrepancies in the timing of inferred vegetation and climate change between these records could be due to real variability in this topographically complex region (Barron et al., 2012; Metcalfe et al., 2015) but could also be related to comparing different record types with different sample resolution. Nonetheless, it is reasonable to infer that $\delta^{18}O_{soil-water}$ was driven by increased aridity between the Early and Mid-Holocene due to a combination of decreased summer rainfall and higher temperature.

It is noteworthy that all of these records suggest that changes in vegetation occurred in concert with increasing summer aridity. However, despite increased summer aridity between the Early and Mid-Holocene, a summer rainfall regime must have persisted to support C_4 vegetation. We recognize that the present $\delta^{18}O_{soil-water}$ dataset cannot be unambiguously parsed into individual effects from rainfall temperature, evaporation intensity, infiltration seasonality, and/or moisture source. We therefore cannot fully understand the complex relationships between changes in vegetation structure due to temperature, rainfall, soil aridity, and other drivers. However, the potential exists to assess individual $\delta^{18}O_{soil-water}$ drivers using soil carbonate rinds and test relationships between environmental conditions and dominant plant photosynthetic pathway through time (see *4.3.2. Avenues for exploration*).

4.2. Coherent connections to the western USA and Mexico

Our interpretation is generally consistent with changes in western USA climate and vegetation interpreted from other records. For example, low elevation records in the Great Basin have been interpreted as indicative of warm and/or wet conditions in the Early Holocene changing to drying and/or warming conditions in the Early- to Mid-Holocene (e.g., Steponaitis et al., 2015; Schuman and Serravezza, 2017). These climate changes were accompanied by vegetation changes; xeric species replaced more mesic ones from ≈13–4 ka, but wetter conditions in the last few millennia apparently supported more mesic plants and increasingly freshwater aquatic communities (Madsen et al., 2001; Schmitt and Lupo, 2012). Similarly, on the Colorado Plateau, Early Holocene forests had expanded ranges associated with wet conditions and a transition to drier summers occurred between 8.6–6 ka (Coats et al., 2008; Morris et al., 2013; Metcalfe et al., 2015). Wetter conditions resumed during the Mid- to Late Holocene, with records documenting increasing water availability between 6.5–4.4 ka.

Regions affected by the NAM show spatial coherence during the Holocene (Metcalfe et al., 2015) and the Torrey record's apparent inverse correlation with more southerly records is a useful indication that it is linked to larger NAM dynamics. For example, in southern New Mexico, vegetation composition ($\%C_3$–plants) was inferred from a sequence of buried soils containing pedogenic carbonate (Cole and Monger, 1994; Monger et al., 1998). Although the time resolution of this record is accordingly constrained to the resolution of individual soil units, the authors inferred that vegetation switched from a dominantly C_4 to

a dominantly C_3 landscape starting around 9–7 ka (from ≈10–30 $\%C_3$–plants to ≈60–80 $\%C_3$–plants). Similar trends were inferred between the LGM and Holocene (from ≈40–50 $\%C_3$–plants to ≈80–90 $\%C_3$–plants) from soils in southern Arizona (Liu et al., 1996). These switches occurred at approximately the same time, but were opposite in direction, to our inferred onset of C_3 plant decline in Torrey (Fig. 6). However, note that at both of these study sites C_3-dominated plant communities (desert scrub) occupy warmer, lower elevation sites than C_4-dominated communities (grasslands). Therefore, while the inferred changes in $\%C_3$–plants between these sites and Torrey are opposite in direction, they may actually represent a coherent response to temperature perturbation (Liu et al., 1996). Thus, in addition to the timing of change, the opposite direction of signals supports the idea that regional vegetation drivers, like temperature, can override global drivers, like CO_2, in determining western USA vegetation composition (Liu et al., 1996; Ehleringer and Monson, 1993; Holmgren et al., 2007; Morris et al., 2013; Schmitt and Lupo, 2012).

Torrey $\delta^{18}O_{soil-water}$ also correlates with Holocene hydrologic records. For example, Torrey $\delta^{18}O_{soil-water}$ inversely correlates with the $\delta^{18}O_{speleothem}$ record from Pink Panther Cave, southern New Mexico, which has been argued to be related to the strength of the NAM or the location of its moisture sources (Fig. 7; Asmerom et al., 2007; Barron et al., 2012). It also inversely correlates with USA Rocky Mountain lake levels (region defined as 30–47.5 °N, 105–112.5 °W; Schuman and Serravezza, 2017). While the exact interpretation of $\delta^{18}O_{soil-water}$, $\delta^{18}O_{speleothem}$, and lake level changes is complex, the correlation between all records supports our interpretation of connections between Torrey soil carbonate and wider western USA hydrologic change.

It is not our goal here to disentangle the intricate climate connections between different sub–regions of the western USA with a single record (Barron et al., 2012; Metcalfe et al., 2015; Schuman and Serravezza, 2017). Rather, we note that our independent climate and vegetation reconstruction is consistent with local records and that the observed inverse correlations between our southern Utah soil carbonate record and other regional records speak to the more general teleconnections inferred for sites in the western USA during the Holocene. Thus, we conclude that laminated soil carbonate records can be used to reconstruct paleoclimate and paleovegetation.

4.3. The soil carbonate paleoarchive

The utility of laminated soil carbonate rinds to provide high-resolution (100 s yr/sample) paleoclimate and vegetation information has broad implications. The key strengths of this methodology are in (1) its dateable stratigraphy, (2) the long record length (10–100 s kyr), (3) the prevalence of soil carbonate rinds in the arid and semi–arid regions that cover ≈30% of Earth's surface, (4) the acquisition of vegetation ($\delta^{13}C_{sc}$) and climate ($\delta^{18}O_{sc}$) information from a single, internally consistent record, and (5) the immediate connection between soil conditions and overriding climate and vegetation, which is enabled by the record's short hydrologic flow path (≈1–m^2 footprint). Laminated soil carbonate rinds thus offer a way to provide new soils perspectives and supplement existing paleoclimate information. In this final section we outline the key strengths of the laminated rind methodology compared to traditional soil carbonate analysis methods, propose ways to improve the laminated rind methodology, and end with a discussion of future avenues of exploration using laminated soil carbonate rinds.

4.3.1. Improved analysis and interpretation of rinds

Studies making use of the laminated soil carbonate proxy thus far have documented several issues that should be addressed to allow robust interpretation. In the field, samples should be selected for the specific question at hand. In general, this will mean that samples should be collected from a single depth within a stable deposit to allow for inter–sample comparison, minimize the influence of atmospheric CO_2 on $\delta^{13}C_{soil-CO2}$ (Cerling, 1984), and mitigate the effect of evaporation on $\delta^{18}O_{soil-water}$ (e.g., Oerter and Amundson, 2016; Huth et al., 2019; Breecker et al., 2009). Modern calibration studies investigating, for example, the annual changes in soil respiration, soil moisture, soil temperature, $\delta^{13}C_{soil-respiration}$, and $\delta^{18}O_{soil-water}$ should be conducted to understand when modern soil carbonate forms and what conditions might potentially have existed in the past. These can be combined with soil temperature reconstructions to constrain the timing of soil carbonate formation throughout the length of a record, which is foundational to quantitatively reconstructing vegetation regimes and $\delta^{18}O_{soil-water}$.

For paleorecord construction, future studies should focus on the scale of sampling, finer–scale age models, and replication. While the rind used in this study was > 1 cm in length, other rinds record 10–100 s ka of environmental change over a mm scale (Oerter et al., 2016; Pustovoytov et al., 2007a, 2007b). Therefore, micromilling subsamples for stable isotope analysis can severely dampen the true signal and should only be used for preliminary screening. Instead, studies should take advantage of the extremely small spatial resolution of SIMS analyses (≈10 μm diameter × 1 μm deep). Because samples may have small-scale variability (e.g., lamination curvature, silicate grains, void spaces, carbonate nodules), microscopic imaging techniques will be useful in determining suitable regions for SIMS analyses. To acquire finer–scale samples for dating, studies can use laser ablation U/Th methodologies where feasible (Oerter et al., 2016). Additionally, finer–scale sampling for radiocarbon dating should also be achievable as ≈1–mg analyses are now possible (Bard et al., 2015). Finally, replication of records from different rinds at a single site (i.e., same soil, depth, and age range but different locations) has not yet been robustly tested to our knowledge (this study, Oerter et al., 2016; Pustovoytov et al., 2007a, 2007b). Future studies that constrain the variability within single soils will make the resulting paleoclimate reconstructions more reliable. Increased automation and concomitant rate of SIMS analysis will be especially useful in achieving this goal (Orland et al., 2019).

4.3.2. Avenues for exploration

Because soil carbonate is common throughout arid and semi–arid soil profiles, the laminated rind methodology presents new avenues for paleoclimate exploration. Studies can now investigate specific landforms of interest (terraces, debris flows, alluvial fans, etc.) which were previously challenging to investigate except by records with low resolution (>1 kyr/sample) and/or time–averaging issues (e.g., packrat middens, bulk soil samples). In addition to assessing the effect of slope, aspect, and topography on vegetation change within a single overarching climate regime, archeologists can use laminated soil carbonate rinds to reconstruct soil conditions at ancient human occupation sites (Pustovoytov et al., 2007a, 2007b). Because soil carbonate rinds are common and result from an extremely small flowpath (≈1–m^2 footprint), it should be feasible to directly compare this single record type in regional sequences, for example across the western USA. It should also be possible to test for elevation–dependent response to climate change by analyzing a sequence of soil carbonate rinds along an elevation transect. As demonstrated in this study, the intensity of soil evaporation is likely to be a significant contributor to $\delta^{18}O_{sc}$ and therefore reconstructed $\delta^{18}O_{soil-water}$. Future studies should test the possibility of reconstructing profiles of $\delta^{18}O_{soil-water}$, and thus constrain evaporative intensity, by comparing several soil carbonate rind records from different soil depths at a single site. Assessing moisture conditions might also be possible via triple oxygen isotopes ($\Delta^{17}O$) or examining elemental ratios of soil carbonate and its included material through time in a single rind (Passey et al., 2014). Finally, by selecting soil carbonate rinds from deeper depths, it may be possible to reconstruct mean annual air temperature through time (Harris and Chapman, 1997).

In addition to the possibilities for climate and vegetation reconstruction from soil carbonate rinds alone, combining this record type with other records can help to create more complete histories. For example, fossil records (pollen in lake cores, packrat middens) can have low resolution (>1 kyr/sample) and, in some cases, underestimate the abundance of vegetation (Betancourt et al., 1990). By combining fossil vegetation reconstructions with the overall landscape vegetation composition (%C_3–plants) available from soil carbonate records, it should be possible to create more detailed (100 s yr/sample) reconstructions of vegetation and vegetation change through time (Cole and Monger, 1994; Liu et al., 1996). Paleovegetation reconstruction from rind $\delta^{13}C_{sc}$ may also be improved by adding information from included organic matter (i.e., $\delta^{13}C_{organic-matter}$) and phytoliths (Cerling, 1984; Hyland et al., 2019).

Soil carbonate rinds may also provide complementary information to speleothem data. For example, one source of C in speleothems is soil–respired CO_2, but $\delta^{13}C_{speleothem}$ data is rarely used to reconstruct $\delta^{13}C_{vegetation}$. This is because along its flow path to eventual speleothem formation, the $\delta^{13}C$ composition of dissolved inorganic carbon can be modified by many processes (e.g., water–rock interactions and kinetic processes during degassing). Records of $\delta^{18}O_{speleothem}$ records are generally interpreted as largely resulting from climate signals, but demonstrating minimal kinetic effects can be difficult (e.g., Dorale and Liu, 2009). In contrast, soil carbonate is generally regarded to form in isotopic equilibrium with soil water and CO_2 (Cerling, 1984). Therefore, assessing extremely high–resolution speleothem isotope data (often < 10 yr/sample) in the context of a nearby soil carbonate record might allow assessment of kinetic effects on $\delta^{13}C_{speleothem}$ through time. In turn, because $\delta^{18}O_{speleothem}$ records can be less sensitive to evaporation occurring within soils than $\delta^{18}O_{sc}$ records, complementary datasets might be used to assess the effect of climate change on vegetation regimes at a single site. Finally, the sensitivity of each proxy is an important consideration. Even where $\delta^{13}C_{speleothem}$ data is not unduly influenced by kinetic effects, such records may not respond to changes in C_4 plant abundance due to differences in C_3-C_4 plant rooting depth (Breecker et al., 2012b). In such cases, soil carbonate records will inherently provide a more robust dataset for reconstructing paleovegetation changes.

5. CONCLUSION

As demonstrated at a site in Torrey, southern Utah, the emerging laminated soil carbonate proxy provides a record of climate and vegetation changes over 10 s ka. Interpreted vegetation (%C_3–plants) and hydrologic ($\delta^{18}O_{soil-water}$) changes agree with interpretations from local pollen records. In addition, the Torrey records correlate with other regional records of vegetation and hydrologic change, demonstrating spatial patterns in line with those previously inferred for the western USA and wider North American Monsoon region (Barron et al., 2012; Metcalfe et al., 2015; Schuman and Serravezza, 2017). We conclude that 10–100 s kyr of sub-millennial scale paleoclimate information (%C_3–plants and $\delta^{18}O_{soil-water}$) can be independently discerned from soil carbonate records if (1) soil system information is available to constrain the modern conditions of soil carbonate formation and (2) the conditions of soil carbonate formation can be constrained through time. Enhanced analytical capabilities related to fine–scale isotope composition sampling will enable more detailed datasets with better age models and will improve interpretations. The laminated soil carbonate proxy presents opportunities for geologists, ecologists, soil scientists, and archeologists to assess the development and interactions of landforms, vegetation, climate, and humans over 10 s–100 s ka in sites that are currently underconstrained or that were previously unfeasible for paleorecord development.

ACKNOWLEDGEMENTS

The authors thank Jay Quade for the use of his CO_2 extraction and graphitization line. We also thank Dan Breecker and an anonymous reviewer for their helpful critiques. TEH thanks Julia Kelson for applying the ^{17}O correction to clumped isotope data. This work made use of University of Utah Shared facilities of the Surface Analysis and Nanoscale Imaging group sponsored by the College of Engineering, Health Sciences Center, Office of the Vice

President for Research, and the Utah Science Technology and Research (USTAR) Initiative of the State of Utah.

FUNDING

This work was supported by NSF grants (EAR 1325214 and 1325225) to TEC, DPF, DWM, and ALE and by the following sources to TEH: NSF grant EF 1137336, University of Utah Geology and Geophysics grants (David S. and Inga M. Chapman Fund; Student Research Fund), a University of Utah Global Change and Sustainability Center grant, and funds from the University of Utah Geochemistry Laboratory and the Environmental Education and Research Fund. A GSA Gladys W. Cole award to DWM partially supported this research. WiscSIMS is supported by NSF (EAR1658823) and the University of Wisconsin. JWV is funded by DOE, Office of Basic Energy Sciences, Geosciences Division (DEFG0293ER14389).

DECLARATION OF COMPETING INTEREST

The authors declare no competing interests.

DATA AND MATERIALS AVAILABILITY

All data are available in the SI Appendix. Samples are housed at the University of Utah and available upon request.

APPENDIX A. SUPPLEMENTARY DATA

Supplementary data to this article can be found online at https://doi.org/10.1016/j.gca.2020.05.022.

REFERENCES

Affek H. P. and Zaarur S. (2014) Kinetic isotope effect in CO_2 degassing: Insight from clumped and oxygen isotopes in laboratory precipitation experiments. *Geochim. Cosmochim. Acta* **143**, 319–330.

Anderson R. S., Betancourt J. L., Mead J. I., Hevly R. H. and Adam D. P. (2000) Middle- and late-Wisconsin paleobotanic and paleoclimatic records from the southern Colorado Plateau, USA. *Palaeo* **155**, 31–57.

Asmerom Y., Polyak V., Burns S. and Rassmussen J. (2007) Solar forcing of Holocene climate: New insights from a speleothem record, southwestern United States. *Geology* **35**, 1–4.

Bard E., Tuna T., Fagault Y., Bonvalot L., Wacker L., Fahrni S. and Synal H.-A. (2015) AixMICADAS, the accelerator mass spectrometer dedicated to ^{14}C recently installed in Aix-en-Provence, France. *Nuclear Inst. Meth. Phys. Res. B* **361**, 80–86.

Barron J. A., Metcalfe S. E. and Addison J. A. (2012) Response of the North American monsoon to regional changes in ocean surface temperature. *Paleocean.* **27**, 1–17.

Bereiter B., Eggleston S., Schmidt J., Nehrbass-Ahles C., Stocker T. F., Fischer H., Kipfstuhl S. and Chappellaz J. (2015) Antarctic Ice Cores Revised 800KYr CO_2 Data. *Geophys. Res. Lett.* **42**(2), 542–549.

Betancourt J. L., Van Devender T. R. and Martin P. S. (1990) *Packrat middens: The last 40,000 years of biotic change*. The University of Arizona Press, Tucson, AZ, USA.

Birkeland P. W., Machette M. N. and Haller K. M. (1991) Soils as a tool for applied Quaternary geology. *Utah Geol. Surv., Vol. Miscellaneous Publ.* **91–3**, 1–63.

Blaauw M. and Christen J. A. (2011) Flexible paleoclimate age-depth models using an autoregressive gamma process. *Bay. Anal.* **6**, 457–474.

Bonifacie M., Calmels D., Eiler J. M., Horita J., Chaduteau C., Vasconcelos C., Agrinier P., Katz A., Passey B. H., Ferry J. M. and Bourrand J.-J. (2017) Calibration of the dolomite clumped isotope thermometer from 25 to 350 °C, and implications for a universal calibration for all (Ca, Mg, Fe)CO_3 carbonates. *Geochim. Cosmochim. Acta* **200**, 255–279.

Bowling D. R., McDowell N. G., Bond B. J., Law B. E. and Ehleringer J. R. (2002) ^{13}C content of ecosystem respiration is linked to precipitation and vapor pressure deficit. *Oecologia* **131**, 113–124.

Breecker D. O. (2017) Atmospheric pCO_2 control on speleothem stable carbon isotope compositions. *Ear. Plan. Sci. Lett.* **458**, 58–68.

Breecker D. O., McFadden L. D., Sharp Z. D., Martinez M. and Litvak M. E. (2012a) Deep autotrophic soil respiration in shrubland and woodland ecosystems in central New Mexico. *Ecosystems* **15**, 83–96.

Breecker D. O., Payne A. E., Quade J., Banner J. L., Ball C. E., Meyer K. W. and Cowan B. D. (2012b) The sources and sinks of CO_2 in caves under mixed woodland and grassland vegetation. *Geochim. Cosmochim. Acta* **96**, 230–246.

Breecker D. O., Sharp Z. D. and McFadden L. D. (2009) Seasonal bias in the formation and stable isotopic composition of pedogenic carbonate in modern soils from central New Mexico, USA. *Geol. Soc. Am. Bull.* **121**(3–4), 630–640.

Cerling T. E. (1984) The stable isotopic composition of modern soil carbonate and its relationship to climate. *Ear. Plan. Sci. Lett.* **71**, 229–240.

Cerling T. E. and Harris J. M. (1999) Carbon isotope fractionation between diet and bioapatite in ungulate mammals and implications for ecological and paleoecological studies. *Oecologia* **120**, 347–363.

Coats L. L., Cole K. L. and Mead J. I. (2008) 50,000 years of vegetation and climate history on the Colorado Plateau, Utah and Arizona, USA. *Quat. Res.* **70**, 322–338.

Cole D. R. and Monger H. C. (1994) Influence of atmospheric CO_2 on the decline of C4 plants during the last deglaciation. *Nature* **368**, 533–536.

Cole K. L., Henderson N. and Shafer D. S. (1997) Holocene vegetation and historic grazing impacts at Capitol Reef National Park reconstructed using packrat middens. *Great Basin Nat.* **57**(4), 315–326.

Coplen T. B. (2007) Calibration of the calcite–water oxygen-isotope geothermometer at Devils Hole, Nevada, a natural laboratory. *Geochim. Cosmochim. Acta* **71**(16), 3948–3957.

Davidson G. (1995) The stable isotopic composition and measurement of carbon in soil CO_2. *Geochim. Cosmochim. Acta* **59**(12), 2485–2489.

Defliese W. F., Hren M. T. and Lohmann K. C. (2015) Compositional and temperature effects of phosphoric acid fractionation on Δ_{47} analysis and implications for discrepant calibrations. *Chem. Geol.* **396**, 51–60.

Dennis K. J., Affek H. P., Passey B. H., Schrag D. P. and Eiler J. M. (2011) Defining an absolute reference frame for 'clumped' isotope studies of CO_2. *Geochim. Cosmochim. Acta* **75**, 7117–7131.

Diefendorf A. F., Mueller K. E., Wing S. L., Koch P. L. and Freeman K. H. (2010) Global patterns in leaf ^{13}C discrimination and implications for studies of past and future climate. *Proc. Natl. Acad. Sci. USA* **107**(13), 5738–5743.

Dorale J. A. and Liu Z. (2009) Limitations of Hendy test criteria in judging the paleoclimatic suitability of speleothems and the need for replication. *J. Cave Karst Stud.* **71**(1), 73–80.

Eggleston S., Schmitt J., Bereiter B., Schneider R. and Fischer H. (2016) Evolution of the stable carbon isotope composition of atmospheric CO_2 over the last glacial cycle. *Paleocean.* **31**, 434–452.

Ehleringer J. R., Cerling T. E. and Helliker B. R. (1997) C_4 photosynthesis, atmospheric CO_2, and climate. *Oecologia* **112**, 285–299.

Ehleringer J. R. and Monson R. K. (1993) Evolutionary and ecological aspects of photosynthetic pathway variation. *Ann. Rev. Eco. Syst.* **24**, 411–439.

Eiler J. (2007) "Clumped-isotope" geochemistry - The study of naturally-occurring, multiply-substituted isotopologues. *Ear. Plan. Sci. Lett.* **262**, 309–327.

Gazis C. and Feng X. (2004) A stable isotope study of soil water: evidence for mixing and preferential flow paths. *Geoderma* **119**, 97–111.

Ghosh P., Adkins J., Affek H., Balta B., Guo W., Schauble E. A., Schrag D. and Eiler J. M. (2006) ^{13}C–^{18}O bonds in carbonate minerals: A new kind of paleothermometer. *Geochim. Cosmochim. Acta* **70**, 1439–1456.

Gile L. H., Peterson F. F. and Grossman R. B. (1996) Morphological and genetic sequences of carbonate accumulation in desert soils. *Soil Sci.* **101**, 347–360.

Hare V. J., Loftus E., Jeffrey A. and Ramsey C. (2018) Atmospheric CO_2 effect on stable carbon isotope composition of terrestrial fossil archives. *Nat. Comm.* **9**(252), 1–8.

Harris R. N. and Chapman D. S. (1997) Borehole temperatures and a baseline for 20th-century global warming estimates. *Science* **275**, 1618–1621.

Henkes G. A., Passey B. H., Jr A. D., Wanamaker, Jr., Grossman E. L., Ambrose W. G. and Carroll M. L. (2013) Carbonate clumped isotope compositions of modern marine mollusk and brachiopod shells. *Geochim. Cosmochim. Acta* **106**, 307–325.

Higgins R. W., Yao Y. and Wang X. L. (1997) Influence of the North American Monsoon system on the U.S. summer precipitation regime. *J. Climate* **10**, 2600–2622.

Holmgren C. E., Norris J. and Betancourt J. L. (2007) Inferences about winter temperatures and summer precipitation from the Late Quaternary record of C_4 perennial grasses and C_3 desert shrubs in the northern Chihuahuan Desert. *J. Quat. Sci.* **22**(2), 141–161.

Horel, J. et al., 2020. Mesowest. [Online] Available at: https://mesowest.utah.edu/ [Accessed 17 April 2020].

Huth T. E., Cerling T. E., Marchetti D. W., Bowling D. R., Ellwein A. L. and Passey B. H. (2019) Seasonal bias in soil carbonate formation and its implications for interpreting high-resolution paleoarchives: evidence from southern Utah. *JGR Biogeosci.* **124**, 616–632.

Hyland E. G., Sheldon N. D., Smith S. Y. and Strömberg C. A. (2019) Late Miocene rise and fall of C_4 grasses in the western United States linked to aridification and uplift. *Geol. Soc. Am. Bull.* **131**, 224–234.

Kelson J. R., Huntington K. W., Breecker D. O., Burgener L. K., Gallagher T. M., Hoke G. D. and Peterson S. V. (2020) A proxy for all seasons? A synthesis of clumped isotope data from Holocene soil carbonates. *Quat. Sci. Rev.* **234**, 1–18.

Kemp P. R. (1983) Phenological patterns of Chihuahuan Desert plants in relation to the timing of water availability. *J. Ecology* **71**(2), 427–436.

Kim S.-T. and O'Neil J. R. (1997) Equilibrium and non-equilibrium oxygen isotope effects in synthetic carbonates. *Geochim. Cosmochim. Acta* **61**(16), 3461–3475.

Kita N. T., Ushikubo T., Fu B. and Valley J. W. (2009) High precision SIMS oxygen isotope analysis and the effect of sample topography. *Chem. Geol.* **264**, 43–57.

Kohn M. J. (2010) Carbon isotope compositions of terrestrial C3 plants as indicators of (paleo)ecology and (paleo)climate. *Proc. Natl. Acad. Sci. USA* **107**, 19691–19695.

Kohn M. J. (2016) Carbon isotope discrimination in C3 land plants is independent of natural variations in pco_2. *Geochem. Persp. Let.* **2**, 35–43.

Kozdon R., Ushikubo T., Kita N. T., Spicuzza M. and Valley J. W. (2009) Intratest oxygen isotope variability in the planktonic foraminifer N. pachyderma: Real vs. apparent vital effects by ion microprobe. *Chem. Geol.* **258**(3–4), 327–337.

Lachniet M. S., Denniston R. F., Asmerom Y. and Polyak V. J. (2014) Orbital control of western North America atmospheric circulation and climate over two glacial cycles. *Nat. Comm.* **5**, 1–8.

Liu B., Phillips F. M. and Campbell A. R. (1996) Stable carbon and oxygen isotopes of pedogenic carbonates, Ajo Mountains, southern Arizona: implications for paleoenvironmental change. *Palaeogeogr. Palaeoclimatol. Palaeoecol.* **124**, 233–246.

Madsen D. B., Rhode D., Grayson D. K., Broughton J. M., Livingston S. D., Hunt J., Quade J., Schmitt D. N. and Shaver I. I. I. M. W. (2001) Late Quaternary environmental change in the Bonneville basin, western USA. *Palaeogeogr. Palaeoclimatol. Palaeoecol.* **167**, 243–271.

Marchetti D. W. and Cerling T. E. (2005) Cosmogenic ^3He exposure ages of Pleistocene debris flows and desert pavements in Capitol Reef National Park, Utah. *Geomorphology* **67**, 423–435.

Marchetti D. W., Cerling T. E. and Lips E. W. (2005) A glacial chronology for the Fish Creek drainage of Boulder Mountain, USA. *Utah. Quat. Res.* **64**, 263–271.

Marchetti D. W., Harris M. S., Bailey C. M., Cerling T. E. and Berman S. (2011) Timing of glaciation and last glacial maximum paleoclimate estimates from the Fish Lake Plateau, Utah. *Quat. Res.* **75**, 183–195.

McFadden Leslie D. (2013) Strongly dust-influenced soils and what they tell us about landscape dynamics in vegetated aridlands of the southwestern United States. In *The Web of Geological Sciences: Advances, Impacts, and Interactions* (ed. Marion E. Bickford). Geological Society of America. https://doi.org/10.1130/2013.2500(15).

Metcalfe S. E., Barron J. A. and Davies S. J. (2015) The Holocene history of the North American Monsoon: 'known knowns' and 'known unknowns' in understanding its spatial and temporal complexity. *Quat. Sci. Rev.* **120**, 1–27.

Monger H. C., Cole D. R., Gish J. W. and Giordano T. H. (1998) Stable carbon and oxygen isotopes in Quaternary soil carbonates as indicators of ecogeomorphic changes in the northern Chihuahuan Desert, USA. *Geoderma* **82**, 137–172.

Morris J. L., Brunelle A., Munson A. S., Spencer J. and Power M. J. (2013) Holocene vegetation and fire reconstructions from the Aquarius Plateau, Utah, USA. *Quat. Int.* **310**, 111–123.

Nordt L., von Fischer J. and Tieszen L. (2007) Late Quaternary temperature record from buried soils of the North American Great Plains. *Geology* **35**(2), 159–162.

Oerter E. J. and Amundson R. (2016) Climate controls on spatial and temporal variations in the formation of pedogenic carbonate in the western Great Basin of North America. *Geol. Soc. Am. Bull.* **128**(7–8), 1–10.

Oerter E. J., Sharp W. D., Oster J. L., Ebeling A., Valley J. W., Kozdon R., Orland I. J., Hellstrom J., Woodhead J. D., Hergt J. M., Chadwick O. A. and Amundson R. (2016) Pedothem carbonates reveal anomalous North American atmospheric

circulation 70000–55000 years ago. *Proc. Natl. Acad. Sci. USA* **113**, 919–924.

Orland, I.J. et al., 2019. An annual-resolution record of deglacial hydroclimate from Hulu Cave, China [abstract]. In: American Geophysical Union, Fall Meeting 2019. 2019 Dec 9–13; San Francisco, CA, AGU; 2019. Abstract PP44B-08.

Oster J. L., Ibarra D. E., Winnick M. J. and Maher K. (2015) Steering of westerly storms over western North America at the Last Glacial Maximum. *Nat. Geosci.* **8**, 201–205.

Passey B. H. and Cerling T. E. (2006) In situ stable isotope analysis ($\delta^{13}C$, $\delta^{18}O$) of very small teeth using laser ablation GC/IRMS. *Chem. Geol.* **235**, 238–249.

Passey B. H., Hu H., Ji H., Montanari S., Li S., Henkes G. A. and Levin N. E. (2014) Triple oxygen isotopes in biogenic and sedimentary carbonates. *Geochim. Cosmochim. Acta* **141**, 1–25.

Prism Climate Group, 2018. PRISM Climate Data. [Online] Available at: http://prism.oregonstate.edu [Accessed 26 January 2018].

Pustovoytov K., Schmidt K. and Parzinger H. (2007a) Radiocarbon dating of thin pedogenic carbonate laminae from Holocene archeological sites. *The Holocene* **17**(6), 835–843.

Pustovoytov K., Schmidt K. and Taubald H. (2007b) Evidence for Holocene environmental changes in the Fertile Crescent provided by pedogenic carbonate coatings. *Quat. Res.* **67**, 315–327.

Quade J. (2014) The carbon, oxygen, and clumped isotopic composition of soil carbonate in archeology. *Treatise Geochem.* **14**, 129–143.

Quade J., Cerling T. E. and Bowman J. R. (1989) Systematic variations in the carbon and oxygen isotopic composition of pedogenic carbonate along elevation transects in the southern Great Basin, United States. *Geol. Soc. Am. Bull.* **101**, 464–475.

Reimer P. J., Bard E., Bayliss A., Beck J. W., Blackwell P. G., Ramsey C., Bronk Buck C. E., Edwards R. L., Friedrich M., Grootes P. M., Guilderson T. P., Haflidason H., Hajdas I., Hatté C., Heaton T. J., Hoffmann D. L., Hogg A. G., Hughen K. A., Kaiser K. F., Kromer B., Manning S. W., Niu M., Reimer R. W., Richards D. A., Scott M. E., Southon J. R., Turney C. and van der Plicht J. (2013) IntCal13 and Marine13 radiocarbon age calibration curves 0–50,000 yr cal BP. *Radiocarbon* **55**(4), 1869–1887.

Romanek C. S., Grossman E. L. and Morse J. W. (1992) Carbon isotopic fractionation in synthetic aragonite and calcite: Effects of temperature and precipitation rate. *Geochim. Cosmochim. Acta* **56**, 419–430.

Schauer A. J., Kelson J., Saenger C. and Huntington K. W. (2016) Choice of ^{17}O correction affects clumped isotope (Δ_{47}) values of CO_2 measured with mass spectrometry. *Rapid Commun. Mass Spectrom.* **30**, 2607–2616.

Schmidt, G.A., Bigg, G.R., Rohling, E.J., 1999. Global Seawater Oxygen-18 Database - v1.22. [Online] Available at: https://data.giss.nasa.gov/o18data/ [Accessed 25 May 2018].

Schmitt D. N. and Lupo K. D. (2012) The Bonneville Estates Rockshelter rodent fauna and changes in Late Pleistocene-Middle Holocene climates and biogeography in the Northern Bonneville Basin USA. *Quat. Res.* **78**, 95–102.

Schubert B. A. and Jahren A. H. (2012) The effect of atmospheric CO_2 concentration on carbon isotope fractionation in C_3 land plants. *Geochim. Cosmochim. Acta* **96**, 29–43.

Schubert B. A. and Jahren A. H. (2018) Incorporating the effects of photorespiration into terrestrial paleoclimate reconstruction. *Earth-Sci. Rev.* **177**, 637–642.

Schuman B. N. and Serravezza M. (2017) Patterns of hydroclimatic change in the Rocky Mountains and surrounding regions since the last glacial maximum. *Quat. Sci. Rev.* **173**, 58–77.

Shurtliff R. A., Nelson S. T., McBride J. H., Rey K. A., Tucker J. C., Godwin S. B. and Tingey D. G. (2017) A 13 000 year multi-proxy climate record from central Utah (western USA), emphasizing conditions leading to mass movements. *Boreas* **46**, 308–324.

Sprenger M., Leistert H., Gimbel K. and Weiler M. (2016) Illuminating hydrological processes at the soil-vegetation-atmosphere interface with water stable isotopes. *Rev. Geophys.* **54**, 674–704.

Steponaitis E., Andrews A., McGee D., Quade J., Hsieh Y.-T., Broecker W. S., Shuman B. N., Burns S. J. and Cheng H. (2015) Mid-Holocene drying of the U.S. Great Basin recorded in Nevada speleothems. *Quat. Sci. Rev.* **127**, 174–185.

Sun Y., Clemens S. C., An Z. and Yu Z. (2006) Astronomical timescale and paleoclimatic implication of stacked 3.6-Myr monsoon records from the Chinese Loess Plateau. *Quat. Sci. Rev.* **25**, 33–48.

Teeri J. A. and Stowe L. G. (1976) Climatic patterns and the distribution of C_4 grasses in North America. *Oecologia* **23**, 1–12.

Teeri J. A., Stowe L. G. and Livingstone D. A. (1980) The distribution of C_4 species of the Cyperaceae in North America in relation to climate. *Oecologia* **47**, 307–310.

Tipple B. J. and Pagani M. (2007) The early origins of terrestrial C_4 photosynthesis. *Annu. Rev. Earth Planet. Sci.* **35**, 435–461.

Treadwell-Steitz C. and McFadden L. D. (2000) Influence of parent material and grain size on carbonate coatings in gravelly soils, Palo Duro Wash, New Mexico. *Geoderma* **94**, 1–22.

Tukey J. W. (1977) *Exploratory Data Analysis*. Addison-Wesley Publishing Co, Reading, MA, USA.

Turnier R. B., Katzir Y., Kitajima K., Orland I. J., Spicuzza M. J. and Valley J. W. (2020) Calibration of oxygen isotope fractionation and calcite-corundum thermometry in emery at Naxos, Greece. *J. Metamorph. Geo.* **38**, 53–70.

Valley J. W. and Kita N. T. (2009) In situ oxygen isotope geochemistry by ion microprobe. In *MAC Short Course: Secondary Ion Mass Spectrometry in the Earth Sciences*, pp. 19–63.

Wentworth T. R. (1983) Distribution of C_4 plants along environmental and compositional gradients in southeastern Arizona. *Vegetatio* **52**, 21–34.

Williford K. H., Ushikubo T., Schopf J. W., Lepot K., Kitajima K. and Valley J. W. (2013) Preservation and detection of microstructural and taxonomic correlations in the carbon isotopic compositions of individual Precambrian microfossils. *Geochim. Cosmochim. Acta* **104**, 165–182.

WiscSIMS, 2020. The Wisconsin Secondary Ion Mass Spectrometer Laboratory. [Online] Available at: http://www.geology.wisc.edu/~wiscsims/ [Accessed 9 May 2020].

Wycech J. B., Kelly D. C., Kozdon R., Orland I. J., Spero H. J. and Valley J. W. (2018) Comparison of $\delta^{18}O$ analyses on individual planktonic foraminifer (Orbulina universa) shells by SIMS and gas-source mass spectrometry. *Chem. Geol.* **483**, 119–130.

Associate editor: F. McDermott